

## Inhomogeneously broadened spin masers

M. V. Romalis\* and W. Happer

Department of Physics, Princeton University, Princeton, New Jersey 08544

(Received 5 February 1999)

Hyperpolarized  $^3\text{He}$  gas, where the nuclear spin polarization has been increased to several tens of percent by optical pumping, can couple such a large negative resistance into an external circuit that masing can ensue. The masing threshold can be suppressed by application of a magnetic field gradient. However, edge enhancement, that is, the less effective diffusional damping of the precessing magnetization at the container walls, can lower the masing threshold. The edge enhancement of the masing is greatly modified by magnetic self-interactions of the spins. [S1050-2947(99)07508-3]

PACS number(s): 33.25.+k, 76.60.Jx, 31.15.-p, 32.80.Bx

### I. INTRODUCTION

Liters of hyperpolarized  $^3\text{He}$  gas with nuclear polarizations of tens of percent and pressures of several atmospheres can be produced by spin-exchange [1] or by metastability exchange [2] optical pumping. The nuclear magnetization of such gases is  $>10^5$  times larger than the thermal-equilibrium magnetization. The  $^3\text{He}$  nucleus has spin quantum number  $K=1/2$  and a negative magnetic moment  $\mu_K < 0$ . Consequently, a  $^3\text{He}$  nucleus with its spin parallel to an applied magnetic field has its magnetic moment antiparallel to the field. Energy can be released by such inverted  $^3\text{He}$  nuclei if the nuclear spins flip and emit Larmor-frequency photons to an external circuit. This potential to emit Larmor-frequency power can be represented by negative resistance in the circuit coupled to the spins. For hyperpolarized gas, the negative resistance of the inverted spins can easily have such a large magnitude that ordinary resistive losses in the circuit are cancelled, and masing can occur.

Larmor-frequency masers with polarized noble gases in nearly uniform magnetic fields have been studied by several groups [3–5]. For a characteristic gradient  $\nabla\omega_L$  of the Larmor frequency  $\omega_L$ , the inhomogeneously broadened magnetic resonance line would have a width of the order  $\delta\omega_L = R|\nabla\omega_L|$ , where  $R$  is a characteristic linear dimension of the cell. For spins with a spatial diffusion coefficient  $D$  the characteristic diffusion rate across the cell is  $D/R^2$ . Previous work on spin masers [3–5] was done in the regime when the diffusion was so fast that  $D/R^2 \gg R\nabla\omega_L$ . In this case the magnetic resonance linewidth is motionally narrowed, and the free-induction decay of spatially uniform, transverse spin polarization is exponential with a time constant [6,7] of the order  $T_2 \propto D/(\nabla\omega_L)^2$ . A detailed theory of maser oscillations for the motional narrowing regime has been given by Richards *et al.* [4].

For current applications of hyperpolarized  $^3\text{He}$  and  $^{129}\text{Xe}$ , for example, polarized targets for nuclear scattering experiments [8], inhaled  $^3\text{He}$  and  $^{129}\text{Xe}$  for magnetic resonance imaging of human lungs and other medical applications

[9–11], or experiments [12] with hyperpolarized liquid  $^{129}\text{Xe}$ , the spins are often in the inhomogeneous broadening regime of large field gradients and slow diffusion, when  $D/R^2 \ll R\nabla\omega_L$ . We report here the results of our theoretical and experimental studies of Larmor-frequency masers in the inhomogeneous broadening regime.

### II. THEORY OF THE INHOMOGENEOUSLY BROADENED SPIN MASER

A sketch of a spin maser in the inhomogeneous broadening regime is shown in Fig. 1. This arrangement is designed to be well described by a one-dimensional theory. It consists of a long right-circular cylinder of length  $2l$  and diameter  $2a$ . The cylinder is filled with polarized gas or liquid and placed inside a resonance coil.

The spin magnetization  $\mathbf{M} = \mathbf{M}(\mathbf{r}, t)$  at the position  $\mathbf{r}$  and time  $t$  will evolve because of precession about the ensemble-averaged magnetic field  $\mathbf{B}^e = \mathbf{B}^e(\mathbf{r}, t)$ , experienced by spins located at  $\mathbf{r}$ , and because of diffusion, as described by

$$\frac{\partial}{\partial t} \mathbf{M} = \gamma \mathbf{B}^e \times \mathbf{M} + D \nabla^2 \mathbf{M}. \quad (1)$$

We use the superscript  $e$  to distinguish the ensemble-averaged field  $\mathbf{B}^e$  from Maxwell's macroscopically averaged field  $\mathbf{B}$ .

Let a coordinate system with orthonormal unit vectors  $x$ ,  $y$ , and  $z$  have its origin at the center of symmetry of the cell.

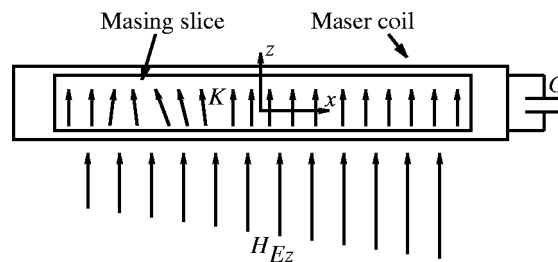


FIG. 1. Schematic of an inhomogeneously broadened spin maser. The magnetization develops a component transverse to the external magnetic field  $H_{Ez}$  only in a thin slice. The magnetic field gradient is greatly exaggerated. The cell has a diameter  $2a$  and length  $2l$ .

\*Present address: Department of Physics, University of Washington, Seattle, WA 98195.

The  $x$  axis is along the cylinder axis. A time-independent and spatially uniform magnetic field  $\bar{H}_{Ez}$  is applied by external coils.  $\bar{H}_{Ez}$  defines the  $z$  axis of the coordinate system, and sets the average Larmor frequency of the spins

$$\bar{\omega}_L = \gamma \bar{H}_{Ez}. \quad (2)$$

The gyromagnetic ratio of the spins is

$$\gamma = -\frac{\mu_K}{\hbar K}, \quad (3)$$

where  $\mu_K$  is the nuclear moment and  $K$  is the spin quantum number. A magnetic field gradient  $\partial H_{Ez}/\partial x$ , created by a separate set of coils, sets the inhomogeneous linewidth of the spin maser.

The spins are initially polarized in the  $z$  direction. The onset of masing is characterized by spontaneous growth of the transverse component of the magnetization, which precesses around the  $z$  axis. The precessing magnetization induces a voltage in the maser coil, which causes a current to flow through the  $LC$  circuit. This current flowing through the coil produces an oscillating magnetic field  $\mathbf{H}_C$ , which drives the precessing spins. The coupling of the spins to the coil is enhanced if the Larmor frequency of the spins is close to the resonance frequency of the  $LC$  circuit. The energy dissipated in the resistance of the coil is provided by transitions of the spins from the high-energy to the low-energy state.

The magnetization generates a macroscopic, irrotational magnetic field  $\mathbf{H}_M$ , the solution of

$$\nabla \cdot \mathbf{H}_M = -4\pi \nabla \cdot \mathbf{M}. \quad (4)$$

The magnetic field  $\mathbf{H}_M$ , which we will call the self-interaction field, has a static component due to the static longitudinal magnetization  $M_z$ , and it has oscillating components due to the oscillating transverse magnetizations  $M_x$  and  $M_y$ . For dense, highly polarized spin samples the gradient,  $\partial H_{Mz}/\partial x$ , of the self-interaction field can be comparable to the applied gradient  $\partial H_{Ez}/\partial x$ , and the oscillating component of  $\mathbf{H}_M$  can be comparable to the oscillating field  $\mathbf{H}_C$  produced by the maser coil. The behavior of spin masers can therefore be strongly influenced by  $\mathbf{H}_M$ , although masing cannot occur in the absence of  $\mathbf{H}_C$ .

To find the masing threshold, it is convenient to represent the effect of the spins by an impedance added in series with the  $LC$  circuit. The total impedance  $Z(\omega)$  of the maser circuit at the angular frequency  $\omega$  is the sum of the series impedance  $Z_C(\omega)$  of the  $LC$  circuit and the impedance  $Z_M(\omega)$  coupled into the circuit from the polarized spins,

$$Z(\omega) = Z_C(\omega) + Z_M(\omega). \quad (5)$$

Approximating the elements of the  $LC$  circuit with a lumped resistance  $R$ , a capacitance  $C$  and an inductance  $L$ , the series impedance of the circuit is

$$Z_C(\omega) = R + i\omega L + \frac{1}{i\omega C}. \quad (6)$$

According to Ohm's law,

$$\tilde{V}(\omega) = \tilde{I}(\omega)Z(\omega), \quad (7)$$

where  $\tilde{V}(\omega)$  and  $\tilde{I}(\omega)$  are, respectively, the temporal Fourier transforms of the externally applied voltage  $V(t)$ , and of the current  $I(t)$  flowing in the circuit. During maser oscillations a nonzero current flows through the circuit with no externally applied voltage, so Eq. (7) implies that the total impedance must vanish,

$$Z(\omega) = Z_C(\omega) + Z_M(\omega) = 0. \quad (8)$$

The solutions  $\omega$  of Eq. (8) may be complex, that is,

$$\omega = \omega' + i\omega'', \quad (9)$$

where the real part of the frequency is  $\omega'$  and the imaginary part is  $\omega''$ . We can distinguish three cases, depending on the value  $\omega''$ . Suppose that a small current  $I(t) = \tilde{I}(\omega)\exp(i\omega t) + \tilde{I}^*(\omega)\exp(-i\omega^*t)$  of frequency  $\omega$  — which satisfies (8) — is initially flowing in the coil. If  $\omega'' < 0$  the amplitude of the coil current will grow exponentially with time as  $e^{|\omega''|t}$ . Even if the coil has no macroscopic current flowing at  $t=0$ , inevitable thermal noise currents can grow exponentially at the frequencies defined by Eq. (8) with  $\omega'' < 0$  until macroscopic oscillations are observed. In this way a transverse, precessing component of the magnetization can develop spontaneously. If a solution of Eq. (8) has  $\omega'' = 0$  then maser oscillations at the frequency  $\omega'$  can persist indefinitely, neither growing nor damping. This is the threshold condition. If a solution of Eq. (8) has  $\omega'' > 0$  then any oscillations damp with time as  $e^{-\omega''t}$ , and the magnetization returns to the longitudinal direction. Thus the masing threshold is given by the solutions of Eq. (8) for which  $\omega'' = 0$ . Masing can commence when a change in the field gradient or some other external parameter of the the system causes a solution  $\omega$  of (8) to move in the complex  $\omega$  plane from above to below the real axis.

In Sec. II A we reduce the fundamental expression (1) to a one-dimensional integro-differential equation suitable for further analysis. In Sec. II B we show how to calculate the spin impedance in the presence of the self-interaction field. We also present simple expressions for the spin impedance and the transverse magnetization for negligible self-interactions ( $\mathbf{H}_M = 0$ ). In Sec. II C we discuss the connection of the spin impedance to the free-induction-decay (FID) transients that can be used for magnetic resonance imaging. In Sec. II D we describe a practical way to calculate the spin impedance when the self-interaction field  $\mathbf{H}_M$  is comparable to the coil field  $\mathbf{H}_C$ .

### A. Spin evolution

The ensemble-averaged magnetic field  $\mathbf{B}^e$  acting on a given  $^3\text{He}$  nucleus is

$$\mathbf{B}^e = \mathbf{H} + \frac{4\pi}{3}\mathbf{M} = \mathbf{H}_E + \mathbf{H}_C + \mathbf{H}_M + \frac{4\pi}{3}\mathbf{M}, \quad (10)$$

where  $\mathbf{H}$  and  $\mathbf{M}$  are the macroscopic magnetic field and magnetization of Maxwell's equations for continuous media. The difference between the effective field of (10) and the macroscopic field  $\mathbf{B} = \mathbf{H} + 4\pi\mathbf{M}$  of Maxwell's equations is due to

the nuclear magnetization excluded from the core of the  $^3\text{He}$  atoms. Equation (10) is closely related to the classical Clausius-Mossotti formulas for dielectrics [15]. The magnetic field  $\mathbf{H}$  consists of the externally applied static magnetic field  $\mathbf{H}_E$ , the alternating magnetic field  $\mathbf{H}_C$  produced by the maser coil, and the field  $\mathbf{H}_M$  produced by the spin magnetization.  $\mathbf{H}_M$  has both static and alternating parts.

The field (10) will be the sum of a static part  $\mathbf{B}_s^e(\mathbf{r})$  and an alternating part  $\mathbf{B}_a^e(\mathbf{r}, t)$ ,

$$\mathbf{B}^e = \mathbf{B}_s^e(\mathbf{r}) + \mathbf{B}_a^e(\mathbf{r}, t). \quad (11)$$

These components are due, respectively, to the static and alternating parts of the external currents and spin magnetization.

The alternating field can be written as a temporal Fourier transform

$$\mathbf{B}_a^e(\mathbf{r}, t) = \int_{-\infty}^{\infty} d\omega \tilde{\mathbf{B}}^e(\mathbf{r}, \omega) e^{i\omega t}. \quad (12)$$

Define a unit vector  $\mathbf{z}$  along the nonzero static field by

$$\mathbf{z} = \frac{\mathbf{B}_s^e}{|\mathbf{B}_s^e|}. \quad (13)$$

We will ignore any spatial variation of the direction  $\mathbf{z}$  over the volume occupied by the spins. The definition (13) ensures that the  $z$  component of the static field is positive,  $B_{sz}^e > 0$ .

The nuclear magnetization of the gas will also be the sum of a static part  $\mathbf{M}_s(\mathbf{r})$  due to the longitudinal spin polarization of the gas, and an alternating part  $\mathbf{M}_a(\mathbf{r}, t)$ , due to the transverse, precessing spin polarization,

$$\mathbf{M} = \mathbf{M}_s(\mathbf{r}) + \mathbf{M}_a(\mathbf{r}, t). \quad (14)$$

In analogy to (12), we can write the alternating part of the magnetization in terms of its Fourier amplitude  $\tilde{\mathbf{M}}(\mathbf{r}, \omega)$

$$\mathbf{M}_a(\mathbf{r}, t) = \int_{-\infty}^{\infty} d\omega \tilde{\mathbf{M}}(\mathbf{r}, \omega) e^{i\omega t}. \quad (15)$$

The static part of the magnetization is

$$\mathbf{M}_s(\mathbf{r}) = \mu_K [\text{He}] P \mathbf{z}, \quad (16)$$

where the spin polarization  $P$  of the gas is related to  $\langle \mathbf{K} \rangle$ , the local expectation value of the nuclear spin, by

$$P = \frac{1}{K} \mathbf{z} \cdot \langle \mathbf{K} \rangle. \quad (17)$$

We assume that  $P$  is independent of position in the volume occupied by the gas.

Substituting (11), (12), (14), and (15) into (1), and retaining only the parts linear in the Fourier amplitudes (since such terms are very small at the onset of masing) we find

$$i\omega \tilde{\mathbf{M}} = \gamma(\mathbf{B}_s^e \times \tilde{\mathbf{M}} + \tilde{\mathbf{B}}^e \times \mathbf{M}_s) + D\nabla^2 \tilde{\mathbf{M}}. \quad (18)$$

We use the unnormalized spherical basis vectors  $\mathbf{x}_{\pm} = \mathbf{x} \pm i\mathbf{y}$  to write the alternating field as

$$\tilde{\mathbf{B}}^e = \frac{1}{2}(\tilde{B}_+^e \mathbf{x}_- + \tilde{B}_-^e \mathbf{x}_+) + \tilde{B}_z^e \mathbf{z}. \quad (19)$$

The precessing magnetization will have negligible longitudinal components, and can therefore be written as

$$\tilde{\mathbf{M}} = \frac{1}{2}(\tilde{M}_+ \mathbf{x}_- + \tilde{M}_- \mathbf{x}_+). \quad (20)$$

Substituting (19) and (20) into (18), we find that the resulting equation has no components proportional to  $\mathbf{z}$ . Noting that  $\pm i\mathbf{z} \times \mathbf{x}_{\pm} = \mathbf{x}_{\pm}$ , and equating the coefficients of  $\mathbf{x}_{\pm}$ , we find

$$[i(\omega \mp \omega_L) - D\nabla^2] \tilde{M}_{\pm} = \pm i\omega_q P \tilde{B}_{\pm}^e, \quad (21)$$

where the local Larmor frequency  $\omega_L$  of the spins is

$$\omega_L = \gamma B_{sz}^e, \quad (22)$$

with the gyromagnetic ratio given by (3). The source frequency is

$$\omega_q = \frac{\mu_K^2}{K\hbar} [\text{He}]. \quad (23)$$

According to (3) and (22)  $^3\text{He}$ , with a negative nuclear moment  $\mu_K < 0$  will have a positive gyromagnetic ratio  $\gamma > 0$  and a positive Larmor frequency,  $\omega_L > 0$ . Then (21) implies that resonant enhancement of  $\tilde{M}_+$  occurs when  $\omega \approx \omega_L$ , when we will have

$$\tilde{M}_+ \gg \tilde{M}_-. \quad (24)$$

In view of (24) we will simply set  $\tilde{M}_- = 0$  in subsequent discussions.

The externally applied magnetic field consists of a spatially uniform magnetic field of magnitude  $\bar{H}_{Ez}$ , and a uniform field gradient  $\partial H_{Ez} / \partial x$ ,

$$\mathbf{H}_E = \left( \bar{H}_{Ez} + x \frac{\partial H_{Ez}}{\partial x} \right) \mathbf{z}. \quad (25)$$

We assume that  $\bar{H}_{Ez}$  is much larger than the static gradient fields and the static fields due to the spin magnetization, so we need only retain the longitudinal components of these smaller fields — the transverse components adding in quadrature to  $\bar{H}_z$  and thus being of negligible significance.

According to the source equation (4), the longitudinal field from the static magnetization  $\mathbf{M}_s$  of the spins is

$$H_{Mz}(\mathbf{r}) = \frac{\partial}{\partial z} \int d^3\mathbf{r}' \frac{\nabla' \cdot \mathbf{M}_s(\mathbf{r}')}{|\mathbf{r} - \mathbf{r}'|} = G \otimes M_{sz} = \mu_K [\text{He}] P G \otimes 1. \quad (26)$$

Here and elsewhere, we use the symbol  $\otimes$  to denote a three-dimensional integral transform, for example,

$$G \otimes M_{sz}(\mathbf{r}) = \int \frac{d^3\mathbf{r}'}{\Omega} G(\mathbf{r}, \mathbf{r}') M_{sz}(\mathbf{r}'). \quad (27)$$

The cylinder volume is  $\Omega = 2\pi a^2 l$ . Integrating (26) by parts, we find that the kernel  $G$  is

$$G(\mathbf{r}, \mathbf{r}') = \Omega \frac{\partial^2}{\partial z^2} \frac{1}{|\mathbf{r} - \mathbf{r}'|}. \quad (28)$$

The spatial Green's function  $G(\mathbf{r}, \mathbf{r}')$  is the product of the cell volume  $\Omega$  and the longitudinal magnetic field  $H_z(\mathbf{r})$  produced by a unit magnetic dipole moment, parallel to the  $z$  axis and located at  $\mathbf{r}'$ .

In accordance with (10), (16), and (26), the longitudinal static field is

$$B_{sz}^e = \bar{H}_{Ez} + x \frac{\partial H_z}{\partial x} + \mu_K[\text{He}]PG \otimes 1 + \frac{4\pi}{3} \mu_K[\text{He}]P. \quad (29)$$

In like manner, we find for the transverse field due to spin magnetization  $\tilde{M}_+$ ,

$$\tilde{H}_{M+} = -2\pi \tilde{M}_+ - \frac{1}{2}G \otimes \tilde{M}_+. \quad (30)$$

From (30) and (10) we find the total effective transverse field

$$\tilde{B}_+^e = \tilde{H}_{C+} - \frac{1}{2}G \otimes \tilde{M}_+ - \frac{2\pi}{3}\tilde{M}_+. \quad (31)$$

The field  $\tilde{H}_{C+}$  is produced by alternating current flowing in the solenoid of Fig. 1. Combining (22), (29), and (31) with (21) we find that  $\tilde{M}_+$  is determined by the integro differential equation

$$i(\omega - \bar{\omega}_L - gx + \omega_q P[G \otimes 1] + 2\pi\omega_q P + \frac{1}{2}\omega_q P G \otimes) \tilde{M}_+ - D\nabla^2 \tilde{M}_+ = i\omega_q P \tilde{H}_{C+}. \quad (32)$$

The Larmor-frequency gradient is

$$g = \gamma \frac{\partial H_{Ez}}{\partial x}. \quad (33)$$

### B. Spin impedance

Let  $V_M = V_M(t)$  be the voltage drop across the solenoid of Fig. 1 due to emission or absorption of radiation by the spins. A current pulse will deposit an amount of energy,

$$E = \int_{-\infty}^{\infty} dt I(t) V_M(t) = 2\pi \int_{-\infty}^{\infty} d\omega |\tilde{I}(\omega)|^2 Z_M(\omega), \quad (34)$$

in the spins. The current is real,  $I(t) = I^*(t)$ , so  $\tilde{I}(-\omega) = \tilde{I}^*(\omega)$ .

The energy  $E$  of (34) is the work done on the oscillating magnetization by the external power sources of the current. Consequently we can write

$$E = \int_{-\infty}^{\infty} dt \int d^3\mathbf{r} \mathbf{H}_C \cdot \frac{\partial}{\partial t} \mathbf{M}. \quad (35)$$

Substituting (15) and (20) into (35) and comparing the result to (34) we conclude that the spin impedance is

$$\begin{aligned} Z_M &= \frac{i\omega}{2|\tilde{I}|^2} \int d^3\mathbf{r} (\tilde{H}_{C-}^* \tilde{M}_- + \tilde{H}_{C+}^* \tilde{M}_+) \\ &= \frac{i\omega}{2|\tilde{I}|^2} \int d^3\mathbf{r} \tilde{H}_{C+}^* \tilde{M}_+. \end{aligned} \quad (36)$$

The last step of (36) follows from (24).

Let us assume that the solenoid of Fig. 1 is ideal and produces a field

$$\tilde{H}_{C+} = \tilde{H}_{C-} = \eta_0 \tilde{I}, \quad (37)$$

where

$$\eta_0 = \frac{4\pi}{c} \frac{dn}{dx}. \quad (38)$$

The number of solenoid windings per unit length is  $dn/dx$ , and  $c$  is the speed of light. Since  $\tilde{H}_{C-}$  is constant in the volume occupied by the spins, it can be taken outside of the integral (36), and the impedance can be written as

$$Z_M = -\frac{\omega WP}{b} \Pi, \quad (39)$$

where the dimensionless impedance coefficient is

$$\Pi = \int_{-1}^1 d\xi \mu, \quad (40)$$

and the dimensionless coordinate is

$$\xi = \frac{x}{l}. \quad (41)$$

The function  $\mu(\xi)$  is a measure of the transverse spin magnetization

$$\mu = \frac{2gl^2}{i\pi\omega_q P \Omega \tilde{H}_{C+}} \int dy dz \tilde{M}_+, \quad (42)$$

generated by the alternating current  $\tilde{I}$ .

The other parameters in (39) are the dimensionless field-inhomogeneity parameter  $b$ ,

$$b = \frac{gl^3}{D}, \quad (43)$$

and the coefficient

$$W = \frac{\hbar K (\pi a \gamma \eta_0)^2 l^3 [\text{He}]}{2D}. \quad (44)$$

The units of  $W$  are  $\text{cm}^{-1} \text{sec}^2$ , the cgs units of inductance. Substituting (42) and (37) into (36), we obtain (39). To convert (39) to SI units, the right-hand side should be multiplied by  $9 \times 10^{11} \text{H cm sec}^{-2}$ .

The function  $\mu$  of (42) is proportional to the average value of  $\tilde{M}_+$  within the cell on a  $yz$  plane located at  $x$ . This suggests that we average (32) in the same way as (42) to find

$$i(\omega - \bar{\omega}_L - gx + 2\pi\omega_q P)\mu - \frac{D}{l^2} \frac{\partial^2 \mu}{\partial \xi^2} + \frac{2gl^2}{\pi\Omega\tilde{H}_{C+}} \times \int dy dz ([G \otimes 1] + \frac{1}{2}G \otimes) \tilde{M}_+ = \frac{gl}{\pi}. \quad (45)$$

Averaging over the diffusive term, we noted the boundary condition at a nondepolarizing cell surface,

$$\mathbf{n} \cdot \nabla M_+ = 0, \quad (46)$$

where  $\mathbf{n}$  is a unit vector normal to the surface. This eliminated the contributions from  $\partial^2 \tilde{M}_+ / \partial z^2$  and  $\partial^2 \tilde{M}_+ / \partial y^2$ .

We will assume that little of the important physics is lost if we ignore the transverse variation of  $\tilde{M}_+$ . This allows us to rewrite (42) as

$$\tilde{M}_+ = \frac{i\omega_q P \Omega \tilde{H}_{C+}}{2gl^2 a^2} \mu. \quad (47)$$

In Eq. (45) we replace the three-dimensional Green's function  $G$  by  $\bar{G}$ , an average over  $yz$  planes, where

$$\bar{G}(x, x') = \frac{1}{\pi^2 a^4} \int dy dz dy' dz' \sigma(a-s) \sigma(a-s') G(\mathbf{r}, \mathbf{r}'). \quad (48)$$

Here

$$\sigma(u) = \begin{cases} 1, & \text{if } u > 0 \\ 0, & \text{otherwise.} \end{cases} \quad (49)$$

is the Heaviside unit step function. The transverse displacement from the  $x$  axis is

$$s = \sqrt{y^2 + z^2}. \quad (50)$$

The approximation (47) is analogous to the atomic Hartree-Fock approximation of using orbitals with well-defined angular momentum, and the approximation (48) is analogous to the Hartree-Fock self-consistent central field approximation. Then (45) becomes

$$i(\omega - \bar{\omega}_L - gx + 2\pi\omega_q P)\mu - \frac{D}{l^2} \frac{\partial^2 \mu}{\partial \xi^2} + i\omega_q P ([\bar{G} \otimes 1] + \frac{1}{2}\bar{G} \otimes) \mu = \frac{gl}{\pi}. \quad (51)$$

Substituting (28) into (48) we find that one factor of the integrand is

$$\Phi(s, x-x') = \int dy' dz' \frac{\sigma(a-s')}{|\mathbf{r}-\mathbf{r}'|}, \quad (52)$$

the potential at the position  $\mathbf{r}$  of a uniformly charged disk of radius  $a$  and of total charge  $\pi a^2$ , located at  $x=x'$ . By symmetry  $\Phi$  depends only on the distance  $|x-x'|$  from the disk along the  $x$  axis, and on the transverse displacement  $s$  of (50). Then (48) becomes

$$\begin{aligned} \bar{G}(x, x') &= \frac{\Omega}{\pi^2 a^4} \int dy dz \sigma(a-s) \frac{\partial^2}{\partial z^2} \Phi(s, x-x') \\ &= \frac{\Omega}{\pi^2 a^5} \frac{\partial \Phi}{\partial s}(a, x-x') \int_{-a}^a dy (z_+ - z_-) \\ &= \frac{\Omega}{\pi a^3} \frac{\partial \Phi}{\partial s}(a, x-x'). \end{aligned} \quad (53)$$

Here the limits of integration along the  $z$  direction are  $z_{\pm} = \pm \sqrt{a^2 - y^2}$ , so the integral on  $dy$  simply gives the area  $\pi a^2$  of a  $yz$  cross section of the cylinder.

For finding  $\partial \Phi / \partial s$  to complete the evaluation of (53) it is convenient to rewrite (52) as

$$\Phi(s, x-x') = 2\pi a \int_0^{\infty} \frac{dk}{k} J_1(ka) J_0(ks) e^{-k|x-x'|}. \quad (54)$$

Here  $J_1$  and  $J_0$  denote Bessel functions. The potential  $\Phi$  defined by (54) is a solution of Laplace's equation  $\nabla^2 \Phi = 0$  if  $\mathbf{r} \neq \mathbf{r}'$ , and for  $\mathbf{r} \rightarrow \mathbf{r}'$  the divergence of  $-\nabla \Phi$  of (54) gives  $4\pi\sigma(a-s)\delta(x-x')$ , the same result as for the potential (52). Both potentials (52) and (54) vanish as  $|x-x'| \rightarrow \infty$  or  $s \rightarrow \infty$ , so they must be identical.

Using (54) with the identity  $J'_0 = -J_1$ , we find,

$$\begin{aligned} \frac{\partial \Phi}{\partial s}(a, x-x') &= -2\pi a \int_0^{\infty} dk J_1^2(ka) e^{-k|x-x'|} \\ &= -2\pi\beta T(\xi - \xi'). \end{aligned} \quad (55)$$

The aspect ratio  $\beta$  of the cell is

$$\beta = a/l, \quad (56)$$

We can use Eq. (11) from Apelblat's tables [16] to write the integral over Bessel functions in (55) as

$$\begin{aligned} T(\xi) &= \frac{1}{\beta} \int_0^{\infty} e^{-|\xi|u/\beta} J_1^2(u) du \\ &= \frac{2}{\pi\beta\sqrt{m}} [(1-m/2)K(m) - E(m)]. \end{aligned} \quad (57)$$

Here the complete elliptic integrals are

$$E(m) = \int_0^{\pi/2} dx \frac{1}{\sqrt{1-m \sin x}}, \quad (58)$$

and

$$K(m) = \int_0^{\pi/2} dx \sqrt{1-m \sin x}. \quad (59)$$

The parameter  $m$  is

$$m = \frac{4\beta^2}{\xi^2 + 4\beta^2}. \quad (60)$$

The self-interaction function  $T$  of (57) depends implicitly on  $\beta$ . Substituting (55) into (53) we find

$$\bar{G}(x, x') = -4\pi T(\xi - \xi'). \quad (61)$$

The three-dimensional integral transforms of (51) reduces to

$$\bar{G} \otimes \mu = -4\pi \int_{-1}^1 \frac{d\xi'}{2} T(\xi - \xi') \mu(\xi') = -4\pi T \star \mu, \quad (62)$$

where the symbol  $\star$  denotes a one-dimensional integral transform as in Eq. (62). Likewise,

$$\bar{G} \otimes 1 = -4\pi T \star 1 = -2\pi F(\xi), \quad (63)$$

where the function  $F$  is

$$F(\xi) = \int_{-1}^1 d\xi' T(\xi - \xi'). \quad (64)$$

Like  $T$ , the function  $F$  depends implicitly on the aspect ratio  $\beta$  of (56). Representative self-interaction functions  $T$  and  $F$  are shown in Fig. 2.

Substituting (62) and (63) into (51) we find

$$i\pi(\rho - X)\mu = 1, \quad (65)$$

where the operator  $X$  is

$$X = \xi - \frac{i}{b} \frac{\partial^2}{\partial \xi^2} + \lambda(F - 1 + T \star). \quad (66)$$

Here the relative frequency is

$$\rho = \frac{\omega - \bar{\omega}_L}{gl}, \quad (67)$$

the self-interaction parameter is

$$\lambda = \frac{2\pi\omega_q P}{gl} = \frac{2\pi\mu_k^2[\text{He}]P}{gl\hbar K}, \quad (68)$$

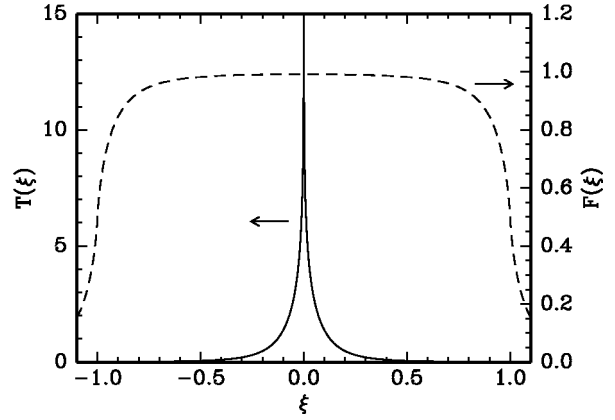


FIG. 2. Self-interaction function  $T(\xi)$  (solid line, plotted against the left axis), and its integral  $F(\xi)$  (broken line, plotted against the right axis). The aspect ratio is  $\beta = a/l = 0.132$ .  $T(\xi)$  can be thought of as the magnetostatic interaction energy [in units of  $2\mu_1\mu_2/(\beta l^3)$ ] of two infinitely thin disks of magnetic moments  $\mu_1$  and  $\mu_2$ , each uniformly magnetized along the  $z$  direction and cut out of the maser cell at the locations  $x_1$  and  $x_2 = x_1 + l\xi$ .

and the other parameters and functions of (66) have been defined above.

Together with the boundary condition

$$\left. \frac{\partial \mu}{\partial \xi} \right|_{\xi = \pm 1} = 0, \quad (69)$$

(65) completely determines the function  $\mu$ .

Before proceeding with the solution of Eq. (65), we briefly consider the limit when  $\lambda \rightarrow 0$ , where spin self-interactions are completely negligible. Physically, this would correspond to low helium density or low spin polarization. In this limit Eq. (65) reduces to an inhomogeneous Airy equation. The solutions are particularly simple when  $|b| \gg 1$  which is true for spin masers far in the inhomogeneous broadening regime. For example, in the experiments discussed in Sec. III, we had  $|b| \approx 10^5$ . For  $b \gg 1$ , the solution of (65) subject to the boundary condition (69) is

$$\mu(\rho, \xi) = b^{1/3} \left\{ \text{Hi}(ib^{1/3}[\xi - \rho]) - e^{2i\pi/3} \frac{\text{Hi}'(ib^{1/3}[-1 - \rho]) \text{Ai}(e^{-i\pi/6} b^{1/3}[\xi - \rho])}{\text{Ai}'(e^{-i\pi/6} b^{1/3}[-1 - \rho])} - e^{-2i\pi/3} \frac{\text{Hi}'(ib^{1/3}[1 - \rho]) \text{Ai}(e^{i\pi/6} b^{1/3}[\rho - \xi])}{\text{Ai}'(e^{i\pi/6} b^{1/3}[\rho - 1])} \right\}. \quad (70)$$

Here and subsequently, fractional powers of positive real numbers, for example  $b^{1/3}$ , will always denote the positive root. For  $b \ll -1$ , one can readily derive an expression analogous to (70), or one can use the symmetry relations summarized in Table I of Sec. II D to show that for  $\lambda = 0$  as assumed in (70),  $\mu(\rho, \xi; -b) = -\mu^*(\rho, \xi; b)$ . The first term of

(70) is proportional to the function  $\text{Hi} = \text{Hi}(z)$ , a standard solution of the inhomogeneous Airy equation  $\text{Hi}'' - z\text{Hi} = 1/\pi$ . An explicit formula for  $\text{Hi}$  is

$$\text{Hi}(z) = \frac{1}{\pi} \int_0^\infty e^{kz - k^3/3} dk. \quad (71)$$

The second and third terms of (70) are needed to ensure the validity of (69). They involve the Airy function  $\text{Ai} = \text{Ai}(z)$ , a standard solution of the homogeneous Airy equation  $\text{Ai}'' - z\text{Ai} = 0$ . An explicit formula for  $\text{Ai}$  is

$$\text{Ai}(z) = \frac{1}{2\pi i} \int_{-i\infty}^{i\infty} e^{zk - k^3/3} dk. \quad (72)$$

From Eq. (42) we see that  $\mu(\rho, \xi)$  is a measure of the transversely averaged, precessing magnetization at the axial location  $x = l\xi$  produced by a coil current oscillating at the frequency  $\omega = \bar{\omega}_L + gl\rho$ . As we shall show in Sec. II C,  $\mu(\rho, \xi)$  is also the amplitude of the free-induction-decay (FID) image at the image space location  $u = l\rho$  of a point source at  $x = l\xi$  in object space. We will therefore call  $\mu(\rho, \xi)$  “the point-spread function.”

Figure 3 shows representative examples of how the function  $\mu(\rho, \xi)$  depends on its arguments  $\rho$  and  $\xi$  for the field-inhomogeneity parameter  $b = 1000$ . The magnetization develops a substantial transverse component only in a thin band with  $\rho \approx \xi$  and with a width of order  $1/b^{1/3}$ . For no self-interactions ( $\lambda = 0$ ) the plots were made using the function (70). The plots for the self-interaction parameter  $\lambda = 0.2$  were made using an eigenfunction expansion discussed in Sec. II D. Note the large asymmetry in  $\mu$  introduced by the self-interactions.

The impedance coefficient  $\Pi = \Pi(\rho)$  can be calculated from the point-spread function with the aid of (40), which implies that  $\Pi$  can also be thought of as the image of an initially uniform distribution of transverse magnetization in the cell. Representative plots of  $\Pi$  are shown in Fig. 4. The peaks near  $\rho = \pm 1$  are due to the edge-enhancement effects commonly observed in magnetic resonance imaging [18–20].

A particularly simple result for the masing threshold can be obtained when the average Larmor frequency  $\bar{\omega}_L$  is exactly equal to the resonance frequency of the masing coil  $2\pi f_C = 1/\sqrt{LC}$ . In this case the coil impedance is  $Z_C = R$ , the real (cgs) resistance of the maser coil at the frequency  $f_C$ . It follows from Eq. (8) and Fig. 4(a) that  $\rho = 0$  and  $\Pi = 1$ . Combining Eqs. (39), (43), and (44) we obtain for the threshold magnetic-field gradient

$$\left. \frac{\partial H_{Ez}}{\partial x} \right|_{\text{th}} = \frac{\omega \pi^2 a^2 \mu_K \eta_0^2}{2R} P[\text{He}]. \quad (73)$$

In this limit the threshold gradient is proportional to the  $^3\text{He}$  polarization and does not depend on the diffusion coefficient  $D$ .

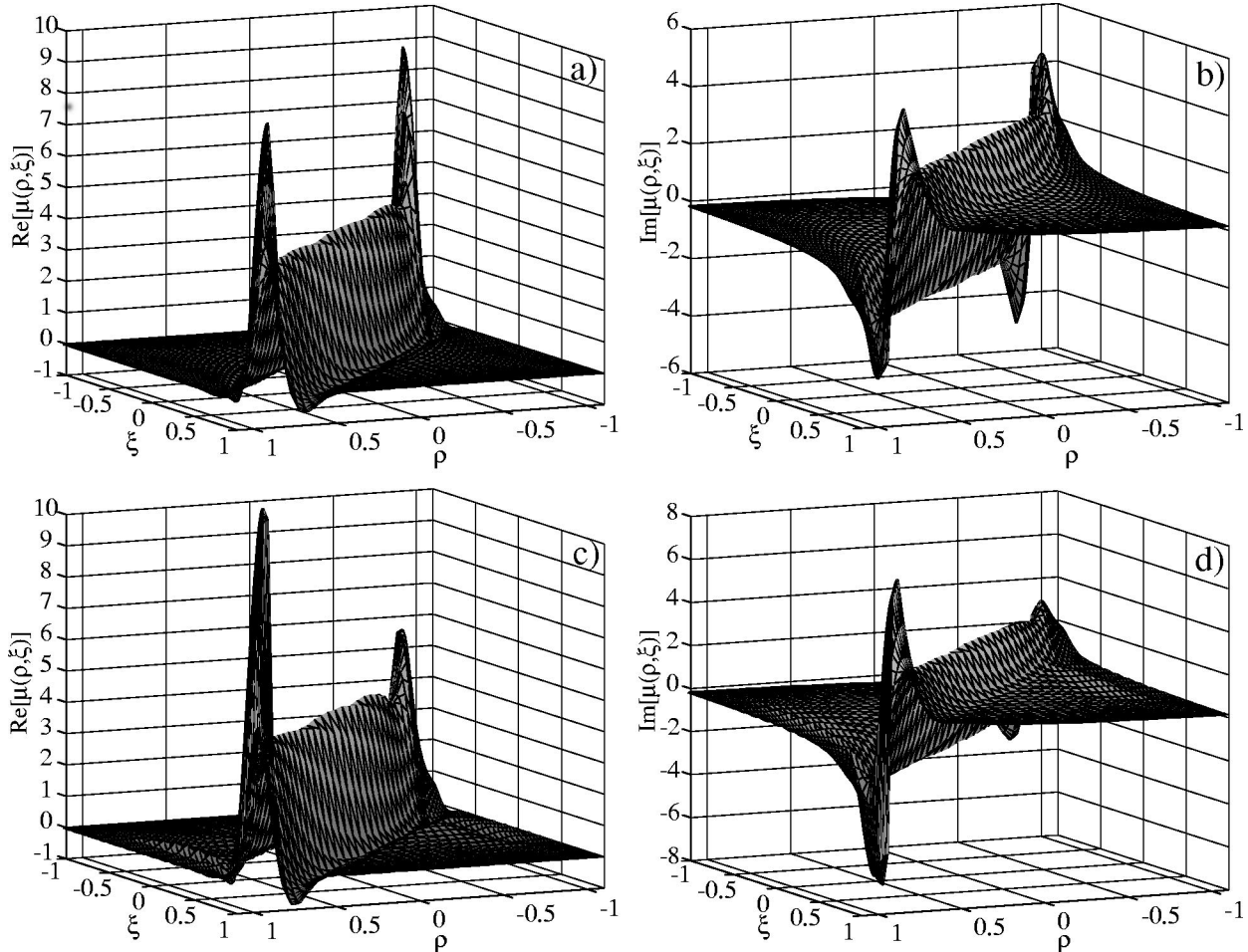


FIG. 3. Point-spread function  $\mu(\rho, \xi)$  for  $b = 1000$ . Plots (a) and (b) show  $\text{Re } \mu(\rho, \xi)$  and  $\text{Im } \mu(\rho, \xi)$ , respectively, in the absence of self-interactions ( $\lambda \rightarrow 0$ ). Plots (c) and (d) show  $\text{Re } \mu(\rho, \xi)$  and  $\text{Im } \mu(\rho, \xi)$ , respectively, for  $\lambda = 0.2$ . The cell aspect ratio is  $\beta = 0.1324$ .

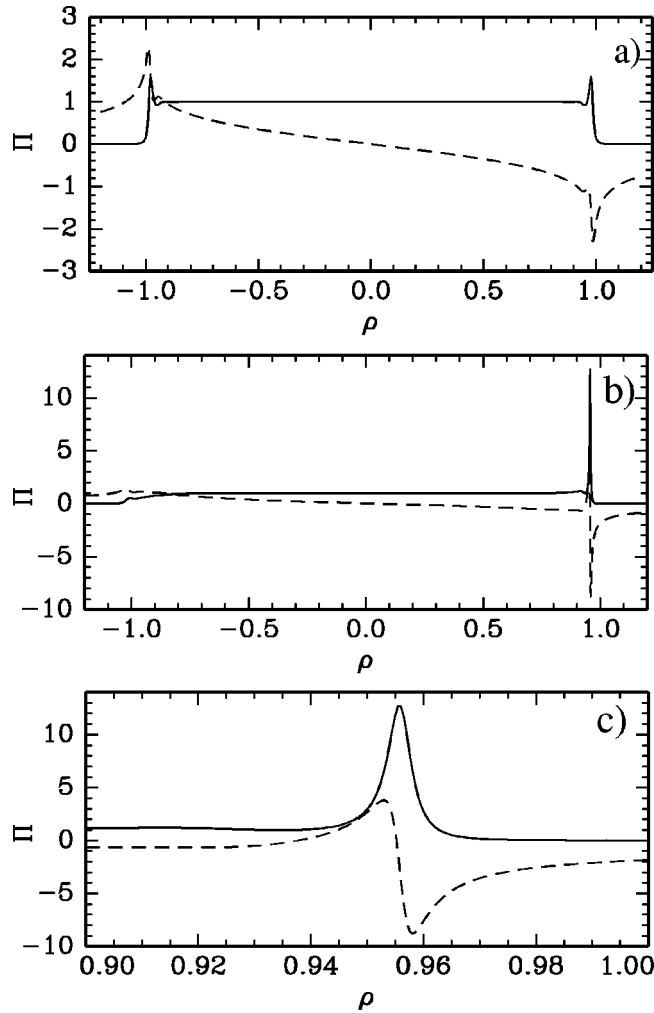


FIG. 4. Impedance coefficient  $\Pi$  ( $\text{Re } \Pi$  solid line;  $\text{Im } \Pi$ , broken line) for (a) no self-interactions and [(b) and (c)] including effects of self-interactions,  $\lambda = 0.122$ ; (c) shows the peak near  $\rho = 1$  of (b) in more detail. Note that for a large range of  $\rho$  between  $-0.8$  and  $0.8$   $\text{Re } \Pi = 1$  with very high accuracy, even in the presence of self-interactions.

### C. Free-induction decay

The spin impedance  $Z_M$  of (34) is closely related to the free-induction-decay (FID) transient, that is, the transient response of spins in which transverse polarization has been generated by a pulse of excitation current in the maser coil. After the excitation pulse ends at  $t=0$  no current is allowed to flow in the maser coil. For example, at  $t=0$  one could replace the capacitor of Fig. 1 with a high-impedance voltmeter. Equating (34), (35), and using (37) we see that the voltage induced in the maser coil by the alternating magnetization is

$$V_M = \eta_0 \int_{\Omega} \frac{\partial M_x(\mathbf{r}, t)}{\partial t} d^3 \mathbf{r}. \quad (74)$$

The FID voltage  $V_M = V_M(t)$  is recorded from  $t=0$  to  $t = \infty$  with a high-impedance voltmeter attached to the maser coil. The one-sided Fourier transform of the FID voltage,

$$\check{V}_M(\omega) = \frac{1}{2\pi} \int_0^{\infty} dt e^{-i\omega t} V_M(t), \quad (75)$$

can be used for magnetic resonance imaging. Substituting (74) into (75), we find

$$\check{V}_M(\omega) = \frac{\eta_0}{2\pi} \int_{\Omega} [i\omega \check{M}_x(\mathbf{r}, \omega) - M_x(\mathbf{r}, 0)] d^3 \mathbf{r}, \quad (76)$$

where

$$\check{M}_x(\mathbf{r}, \omega) = \frac{1}{2\pi} \int_0^{\infty} dt e^{-i\omega t} M_x(\mathbf{r}, t). \quad (77)$$

We take the image of the transverse magnetization to be

$$\begin{aligned} I(\rho) &= \frac{4g}{i\omega \pi a^2 \eta_0} [\check{V}_M(\omega) - \check{V}_M(0)] \\ &= \frac{g}{\pi^2 a^2} \int_{\Omega} \check{M}_+(\mathbf{r}, \omega) d^3 \mathbf{r}, \end{aligned} \quad (78)$$

where  $\rho$  was defined by (67) and  $\check{M}_x = \check{M}_+/2$ . We will presently show that the image (78) can be obtained from the initial transverse magnetization at the start of the FID transient with the help of the point-spread function  $\mu(\rho, \xi)$ ,

$$I(\rho) = \int_{-1}^1 \mu(\rho, \xi) M_+(\rho \xi, 0) d\xi. \quad (79)$$

According to (79),  $\mu(\rho, \xi)$  is the intensity at an image-space point  $\rho$  generated by a point source of magnetization at the object-space point  $\xi = x/l$ . Thus, the function  $\mu$  plays much the same role for diffusion-limited magnetic resonance imaging as the Airy-disk function of a diffraction-limited optical system [17].

During the FID, the current in the coil is assumed to be negligible, so we may modify the arguments leading to (51) to find

$$\begin{aligned} i(\omega - \bar{\omega}_L - gx + \omega_q P[\bar{G} \otimes 1] + 2\pi\omega_q P + \frac{1}{2}\omega_q P\bar{G} \otimes) \check{M}_+ \\ - \frac{D}{l^2} \frac{\partial^2}{\partial \xi^2} \check{M}_+ = M_+. \end{aligned} \quad (80)$$

Here it is to be understood that the initial magnetization  $M_+ = M_+(x, 0)$  and the one-sided Fourier transform  $\check{M}_+ = \check{M}_+(x, \omega)$  are values averaged in the  $yz$  plane. In analogy to (65) we may write (80) for  $g > 0$  as

$$igl(\rho - X)\check{M}_+ = M_+. \quad (81)$$

Define the resolvent of (81) by

$$i(\rho - X)R(\rho; \xi, \xi') = \delta(\xi - \xi'). \quad (82)$$

As we will show in Sec. II D, the resolvent is symmetric in  $\xi$  and  $\xi'$ , that is

$$R(\rho; \xi, \xi') = R(\rho; \xi', \xi), \quad (83)$$

Then the solution to (81) is

$$\check{M}_+(\rho \xi, \omega) = \frac{1}{gl} \int_{-1}^1 R(\rho; \xi, \xi') M_+(\rho \xi', 0) d\xi'. \quad (84)$$

Substituting (84) into (78) we find (79), where the point-spread function defined by (65) is related to the resolvent by

$$\mu(\rho, \xi) = \frac{1}{\pi} \int_{-1}^1 d\xi' R(\rho; \xi', \xi). \quad (85)$$

In view of (40), (85) implies that the impedance coefficient is

$$\Pi(\rho) = \frac{1}{\pi} \int_{-1}^1 d\xi \int_{-1}^1 d\xi' R(\rho; \xi, \xi'). \quad (86)$$

#### D. Pole expansions

We have tested various ways to solve (65), including perturbation theory and iterative methods. As we shall show shortly, it is straightforward to write down an expression for  $Z_M$  as the sum of an infinite number of poles in the complex  $\rho$  plane. The poles are the eigenvalues of the pole-position operator  $X$  of (66). Here we summarize the most successful computational method we have tried, where we write the impedance as the sum of discrete contributions from the  $2m$  most slowly damping poles plus the contribution from the infinite number of remaining poles, which we approximate by an integral over a ‘‘line charge’’ of poles in the complex  $\rho$  plane.

We will use Dirac notation to simplify the subsequent discussion. Let the point-spread function  $\mu$  of (65) be the projection of an abstract vector  $|\mu\rangle$  on a spatial-coordinate basis vector  $|\xi\rangle$ , that is

$$\mu(\rho, \xi) = \langle \xi | \mu \rangle. \quad (87)$$

The abstract vector  $|\mu\rangle$  depends implicitly on the relative frequency  $\rho$ . The position eigenvectors form a complete set in the sense that

$$\langle \xi | \xi' \rangle = \delta(\xi - \xi') \quad (88)$$

and

$$\int_{-1}^1 d\xi |\xi\rangle \langle \xi| = 1. \quad (89)$$

Then (65) is equivalent to

$$i\pi(\rho - X)|\mu\rangle = |1\rangle. \quad (90)$$

The projection of the abstract source vector  $|1\rangle$  on the position eigenvectors is

$$\langle \xi | 1 \rangle = \langle 1 | \xi \rangle = \begin{cases} 1, & \text{if } |\xi| < 1; \\ 0, & \text{otherwise.} \end{cases} \quad (91)$$

The pole-position operator  $X$  can be written as

$$X = X^{(0)} + \lambda X^{(1)}. \quad (92)$$

From inspection of (65), (90), and (92) we conclude that the zeroth-order part of  $X$  is local — that is, diagonal in position — and given by the matrix

$$\langle \xi' | X^{(0)} | \xi \rangle = \delta(\xi' - \xi) \left[ \xi - \frac{i}{b} \frac{d^2}{d\xi^2} \right]. \quad (93)$$

The first-order part of  $X$  has a nonlocal term and is given by

$$\langle \xi' | X^{(1)} | \xi \rangle = \delta(\xi' - \xi) [F(\xi) - 1] + T(\xi' - \xi). \quad (94)$$

We will use parentheses to denote the zeroth-order eigenvectors  $|n\rangle$  of  $X^{(0)}$ , that is

$$X^{(0)}|n\rangle = x_n^{(0)}|n\rangle, \quad (95)$$

and we will use curly brackets to denote the eigenvectors  $|n\rangle$  of  $X$ ,

$$X|n\rangle = x_n|n\rangle. \quad (96)$$

Denote the projections of the eigenvectors of (95) and (96) onto the position eigenvectors  $|\xi\rangle$  by the functions

$$\phi_n(\xi) = \langle \xi | n \rangle \quad (97)$$

and

$$\psi_n(\xi) = \langle \xi | n \rangle. \quad (98)$$

Clearly,  $|n\rangle \rightarrow |n\rangle$  and  $\psi_n \rightarrow \phi_n$  as  $\lambda \rightarrow 0$ .

The abstract eigenvalue equation (96) is equivalent to the integro-differential equation

$$\left[ \xi - \frac{i}{b} \frac{d^2}{d\xi^2} - \lambda(1 - F - T\star) \right] \psi_n = x_n \psi_n. \quad (99)$$

Multiplying (99) by  $\psi_n^*$  and integrating over  $d\xi$  we find that the real and imaginary parts of the pole position can be expressed as

$$\begin{aligned} \text{Re } x_n = & \left[ \int d\xi |\psi_n(\xi)|^2 [\xi + \lambda\{F(\xi) - 1\}] \right. \\ & \left. + \lambda \int d\xi' \int d\xi \psi_n^*(\xi') T(\xi' - \xi) \psi_n(\xi) \right] \\ & \times \left[ \int d\xi |\psi_n|^2 \right]^{-1}, \end{aligned} \quad (100)$$

$$\text{Im } x_n = \left[ \frac{1}{b} \int d\xi \left| \frac{d\psi_n}{d\xi} \right|^2 \right] \left[ \int d\xi |\psi_n|^2 \right]^{-1}. \quad (101)$$

The imaginary part  $\text{Im } x_n$  of the pole location has the same sign as  $b$ . For the eigenfunction  $\psi_n$ , the damping rate of the precessing magnetization by diffusion is proportional to  $|\text{Im } x_n|$ .

From inspection of (65)–(68) we see that certain symmetry relations exist for the sign changes  $b \rightarrow -b$  and  $\lambda \rightarrow -\lambda$ . These are summarized in Table I.

Here subscript  $p$  can be  $l$  (left),  $c$  (center), or  $r$  (right). The conjugate subscripts are  $\bar{l} = r$ ,  $\bar{c} = c$  and  $\bar{r} = l$ . As a simple example of the use of the symmetries in Table I, consider the reversal of the magnetic field gradient,  $g \rightarrow -g$ . As a result we would have  $b \rightarrow -b$ ,  $\lambda \rightarrow -\lambda$  and  $\rho \rightarrow -\rho$ . According to (39) and the symmetries of Table I, changing the sign of the field gradient has no effect on the impedance, so  $Z_M \rightarrow Z_M$ .

Stoller, Happer, and Dyson [21] (SHD) made a detailed study of (95) for magnetic resonance applications. DeSwiet

and Sen [20] showed that the SHD formalism could naturally be used to account for edge enhancements in magnetic resonance imaging. We will use the methods of SHD here, extended to account for magnetic self-interactions, to analyze the masing thresholds.

SHD showed that the eigenfunctions can be chosen to be orthonormal,

$$\int_{-1}^1 d\xi \phi_m(\xi) \phi_n(\xi) = \int_{-1}^1 d\xi (m|\xi)\langle\xi|n\rangle = (m|n) = \delta_{mn}. \quad (102)$$

From inspection of (102), we see that we must define

$$(m|\xi) = \langle\xi|m\rangle = \phi_m(\xi) \quad (103)$$

rather than  $(m|\xi) = \langle\xi|m\rangle^*$ , as would be the case if  $X^{(0)}$  were a Hermitian operator.

SHD (Ref. [21]) also show that the eigenfunctions (97) form a complete basis set, unless  $b$  is one of the ‘‘exceptional’’ values, where pairs of poles coalesce. SHD show how to augment the  $\phi_n$  to make a complete set when  $b$  is one of the exceptional values. Ignoring the rare case that  $b$  is an exceptional value, the orthonormality of the eigenfunctions (97) can be expressed as

$$\sum_n |n\rangle\langle n| = 1. \quad (104)$$

None of the SHD arguments [21] leading to (102)–(104) would change for  $\lambda \neq 0$ , in (99), so we can also assume that

$$\int_{-1}^1 d\xi \psi_m(\xi) \psi_n(\xi) = \int_{-1}^1 d\xi \{m|\xi\rangle\langle\xi|n\rangle = \{m|n\rangle = \delta_{mn} \quad (105)$$

with

$$\{m|\xi\rangle = \langle\xi|m\rangle = \psi_m(\xi), \quad (106)$$

and

$$\sum_n |n\rangle\langle n| = 1. \quad (107)$$

Inserting (107) into (90) we find with the aid of (96)

$$|\mu\rangle = \frac{1}{i\pi} \sum_n \frac{|n\rangle\langle n|1\rangle}{\rho - x_n}. \quad (108)$$

Using (107), (87), (91), and (40), we find that the impedance coefficient is

$$\Pi = \int_{-1}^1 \langle\xi|\mu\rangle d\xi = \int_{-\infty}^{\infty} \langle 1|\xi\rangle\langle\xi|\mu\rangle d\xi = \langle 1|\mu\rangle. \quad (109)$$

Substituting (108) into (109) we find

$$\Pi = \frac{1}{i\pi} \sum_n \frac{\langle 1|n\rangle\langle n|1\rangle}{\rho - x_n}. \quad (110)$$

According to (101) the imaginary part of  $x_n$  has the same sign as  $b$ , so for  $b > 0$  all the poles of (110) lie above the real axis of the complex  $\rho$  plane, and for  $b < 0$  all the poles lie below the real axis. This is in accordance with the causal physics of the Kramers-Kronig relations [13,22], since in either case (39) and (67) ensure that the poles of  $Z_M$  lie above the real axis of the complex  $\omega$  plane.

Integrating (110) along the real axis of the complex  $\rho$  plane, we find for  $\text{sgn}(b) = \pm 1$

$$\begin{aligned} \int_{-\infty}^{\infty} \Pi d\rho &= \pm \sum_n \langle 1|n\rangle\langle n|1\rangle = \pm \langle 1|1\rangle \\ &= \pm \int_{-1}^1 \langle 1|\xi\rangle\langle\xi|1\rangle d\xi = \pm 2. \end{aligned} \quad (111)$$

Stepping through (111) we used (107) and (89) to find that the area of  $\Pi$ , the impedance coefficient, is  $\pm 2$ , depending on the sign of  $b$ . In like manner, one can show that for  $|\xi| \leq 1$ , we have for  $\text{sgn}(b) = \pm 1$

$$\int_{-\infty}^{\infty} \mu(\rho, \xi) d\rho = \pm 1. \quad (112)$$

In other words, the point-spread function may broaden and distort the image of an object point of magnetization located at  $\xi$ , but the integrated area of the image is always  $\pm 1$ , depending on the sign of  $b$ , so no object area is lost.

From inspection of (82) we see that the resolvent is

$$R(\rho; \xi, \xi') = R(\rho; \xi', \xi) = \sum_n \frac{\psi_n(\xi) \psi_n(\xi')}{i[\rho - x_n]}. \quad (113)$$

The expression (110) for the impedance coefficient is an exact solution of (65), but it is not possible to sum over the infinite number of poles. However, for the experimental conditions of most interest, the field inhomogeneity parameter is very large,  $|b| \gg 1$  because of the high gas pressure and the tendency for the cell to mase if the field inhomogeneity is too small. For  $|b| \gg 1$ , SHD (Ref. [21]) showed that the zeroth-order eigenvalues can be classified into complex conjugate pairs, representing localized magnetization precessing to the right ( $r$ ) or left ( $l$ ) of the center plane ( $c$ ) of the cell. There is a total of  $q$  left poles,  $x_{ln}$ , of (110) with  $\text{Re} x_{ln} < 0$  and  $q$

TABLE I. Symmetry properties for sign changes of  $b$  and  $\lambda$ .

$b'$	$\lambda'$	$x_{pn}(b', \lambda')$	$\psi_{pn}(\xi; b', \lambda')$	$\mu(\rho, \xi; b', \lambda')$	$\Pi(\rho; b', \lambda')$
$-b$	$\lambda$	$x_{pn}^*(b, \lambda)$	$\psi_{pn}^*(\xi; b, \lambda)$	$-\mu^*(\rho, \xi; b, \lambda)$	$-\Pi^*(\rho; b, \lambda)$
$b$	$-\lambda$	$-x_{pn}^*(b, \lambda)$	$-\psi_{pn}^*(-\xi; b, \lambda)$	$\mu^*(-\rho, -\xi; b, \lambda)$	$\Pi^*(-\rho; b, \lambda)$
$-b$	$-\lambda$	$-x_{pn}(b, \lambda)$	$-\psi_{pn}(-\xi; b, \lambda)$	$-\mu(-\rho, -\xi; b, \lambda)$	$-\Pi(-\rho; b, \lambda)$

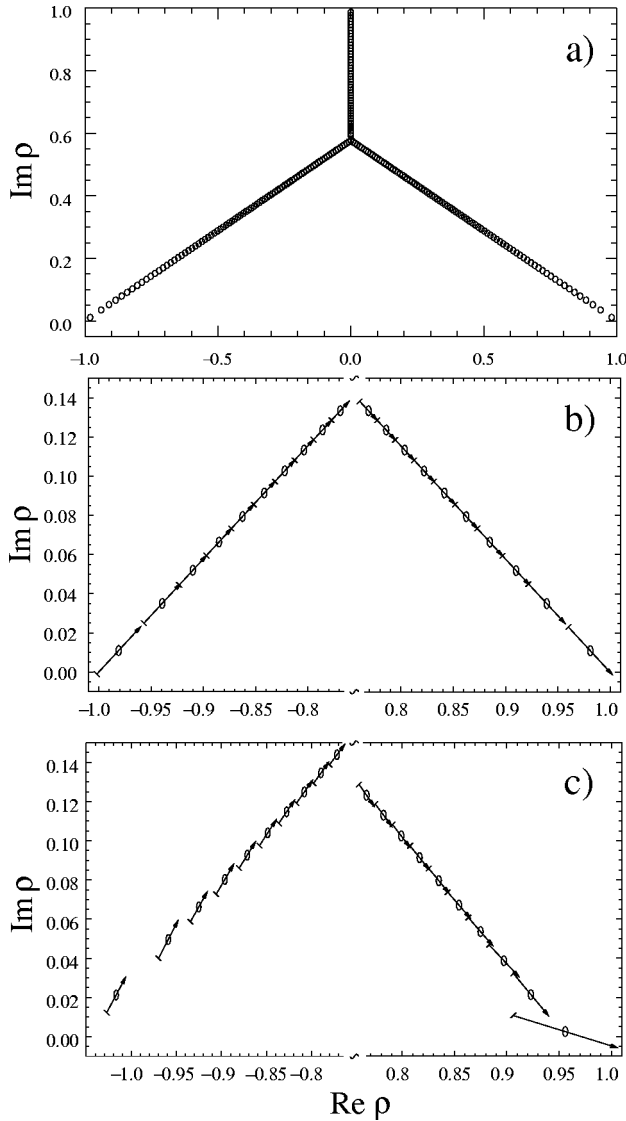


FIG. 5. Locations of the complex poles  $x_n$  (open circles) of  $\Pi(\rho)$  in the complex  $\rho$  plane. Plots (a) and (b) show the poles in the absence of self-interaction, (c) includes self-interaction. Also shown in (b) and (c) are the residues  $\{n|1\}^2$  of  $i\pi\Pi(\rho)$ . The residues are represented by arrows centered on the corresponding poles. The poles and residues are obtained by diagonalization of the matrix given by Eq. (145) for  $b=10^5$ . For (c)  $\lambda=0.122$  was used.

right poles  $x_{rn}$  with  $\text{Re } x_{rn} > 0$ . In addition, there is an infinite number of purely imaginary center poles  $x_{cn}$  with  $\text{Re } x_{cn} = 0$ . The contribution of the center poles to the impedance turns out to be negligible for  $|b| \gg 1$ .

A representative sketch of these poles is shown in Fig. 5(a). They are enumerated with an index  $n=1,2,3,\dots$ , such that low-index poles damp more slowly than high-index poles, for example,  $\text{Im } x_{ln} < \text{Im } x_{l,n+1}$ . The  $m$ -pole approximation consists of picking the  $m$  slowest-damping left and right poles, with  $m \ll q$  and writing (110) as

$$\Pi = \Pi_{lm} + \Pi_{rm} + \Delta\Pi_m, \quad (114)$$

where

TABLE II. First ten zeros of the Airy function derivative  $\text{Ai}'$  and parameters derived from them.

$n$	$-a'_n$	$K_n$	$b_m$
1	1.018 793	2.2393	7.293 38
2	3.248 198	1.8753	45.245 4
3	4.820 099	1.3897	108.317
4	6.163 307	1.2899	203.707
5	7.372 177	1.1434	324.833
6	8.488 487	1.0885	477.631
7	9.535 445	1.0105	656.677
8	10.527 66	0.973 86	866.978
9	11.475 06	0.923 25	1103.87
10	12.384 79	0.896 29	1371.74

$$\Pi_{lm} = \frac{1}{i\pi} \sum_{n=1}^m \frac{\langle 1|ln \rangle^2}{\rho - x_{ln}}, \quad (115)$$

and

$$\Pi_{rm} = \frac{1}{i\pi} \sum_{n=1}^m \frac{\langle 1|rn \rangle^2}{\rho - x_{rn}}. \quad (116)$$

Using (91) and (103) we find that the amplitude in the numerator of (115) is

$$\{n|1\rangle = \langle 1|n\rangle = \int_{-1}^1 d\xi \{n|\xi\rangle \langle \xi|1\rangle = \int_{-1}^1 d\xi \psi_n(\xi). \quad (117)$$

For  $\lambda=0$  and  $b \gg 1$ , SHD (Ref. [21]) showed that the left and right poles are given very nearly by

$$x_{ln}^{(0)} = -x_{rn}^{(0)*} = -1 - a'_n \frac{e^{i\pi/6}}{b^{1/3}}. \quad (118)$$

The corresponding eigenfunctions are

$$\phi_{ln}(\xi) = \phi_{rn}^*(-\xi) = N_{ln} \text{Ai}(a'_n + e^{-i\pi/6}[1+\xi]b^{1/3}), \quad (119)$$

where the normalization coefficient is

$$N_{ln} = \frac{b^{1/6} e^{-i\pi/12}}{\text{Ai}(a'_n)(-a'_n)^{1/2}}. \quad (120)$$

The roots  $a'_n$  of  $\text{Ai}'$ , the Airy-function derivative  $\text{Ai}'(z) = d\text{Ai}(z)/dz$ , are the solutions of

$$\text{Ai}'(a'_n) = 0. \quad (121)$$

Numerical values of  $a'_n$  are given in Table II for  $n \leq 10$ . For  $\lambda=0$  we can substitute (119) into (117) to find

$$\langle ln|1\rangle = \langle rn|1\rangle^* = \frac{e^{i\pi/12}}{b^{1/6}} (K_n)^{1/2}. \quad (122)$$

where positive coefficient  $K_n$

$$K_n = \frac{Zi^2(a'_n)}{-a'_n Ai^2(a'_n)} \tag{123}$$

is listed for  $n \leq 10$  in Table II. In (123) the function  $Zi$ , a negative antiderivative of  $Ai$ , is defined by

$$Zi(z) = \int_z^\infty Ai(z') dz'. \tag{124}$$

The endpoint of the integral is at infinity in the sector  $-\pi/3 \leq \arg z' \leq \pi/3$  where  $Ai(z') \rightarrow 0$  as  $\exp(-2z'^{3/2}/3)$ . We note that for  $z \rightarrow -\infty$  along the real axis,  $Zi(z) \rightarrow 1$ .

For real values of  $z$  which are not too negative,  $Zi(z)$  can be conveniently evaluated from the integral along the positive  $k$  axis

$$Zi(z) = \frac{1}{3} - \frac{1}{\pi} \int_0^\infty \frac{\sin(zk\sqrt{3}/2) \exp(-zk/2 - k^3/3)}{k} dk. \tag{125}$$

This expression can be found by substituting the integral representation (72) into (124), and deforming the path of integration in the complex  $k$  plane to be inward along the ray  $e^{-i\alpha}$ , where  $\alpha = 2\pi/3$ , from  $\infty$  to the small positive radius  $\epsilon$ . Thence the integration continues in a negative sense around a circular arc of radius  $\epsilon$  from the ray  $e^{-i\alpha}$  to the ray  $e^{i\alpha}$  and finally outward along the ray  $e^{i\alpha}$  from  $\epsilon$  to  $\infty$ . Taking the limit of (124) as  $\epsilon \rightarrow 0$  gives (125).

Substituting (122) into (115) we find for  $b \gg 0$  and  $\lambda = 0$ ,

$$\Pi_{lm} = \frac{e^{i\pi/6}}{i\pi b^{1/3}} \sum_{n=1}^m \frac{K_n}{\rho - x_{ln}^{(0)}} \tag{126}$$

and

$$\Pi_{rm} = \frac{e^{-i\pi/6}}{i\pi b^{1/3}} \sum_{n=1}^m \frac{K_n}{\rho - x_{rn}^{(0)}}. \tag{127}$$

The residual terms not included in (115) and (116) make the contribution  $\Delta\Pi_m$  to (114). To evaluate these, we approximate the sum over discrete poles by an integral over a continuous ‘‘line charge’’ of poles. The coefficient  $K_n$  of (123) for  $q \gg n > m \gg 1$  can be found from asymptotic expressions for the Airy functions

$$Ai(z) \sim \frac{1}{\sqrt{\pi(-z)^{1/4}}} \sin\left[\frac{2}{3}(-z)^{3/2} + \frac{\pi}{4}\right],$$

for  $|\arg(-z)| < 2\pi/3$ . (128)

We also use the asymptotic expression for the zeros

$$-a'_n \sim \left[\frac{3}{2}\pi(n-3/4)\right]^{2/3}. \tag{129}$$

Using (128) and (129) with (123) and setting  $Zi(a'_n) \sim 1$  for large  $n$  we find

$$K_n \sim \frac{\pi}{(-a'_n)^{1/2}} = \Delta(-a'_n), \tag{130}$$

where  $\Delta(-a'_n) = -a'_{n+1} + a'_n$ . From Eqs. (118), (126), and (130) we conclude that for large  $n$  the residue of  $i\pi\Pi(\rho)$  is very nearly equal to the displacement of nearest-neighbor poles

$$\langle 1|ln\rangle \langle ln|1\rangle = \frac{e^{i\pi/6}}{b^{1/3}} K_n \rightarrow \Delta x_{ln}^{(0)}. \tag{131}$$

The significance of Eq. (131) is demonstrated in Fig. 5(b), where we show graphically the residues  $\langle 1|ln\rangle \langle ln|1\rangle$  and  $\langle 1|rn\rangle \langle rn|1\rangle$  as rays centered on the poles. One can see that for  $n > 3$  successive residues link the poles with great precision, like the links of a chain. This shows that the sum in Eq. (126) can be accurately replaced by a line integral. Substituting (122) and (131) into (115), we find the left-pole contribution not included in (126) is

$$\Delta\Pi_{lm} = \frac{e^{i\pi/6}}{i\pi b^{1/3}} \sum_{n=m+1}^q \frac{K_n}{\rho - x_{ln}^{(0)}} \rightarrow \frac{1}{i\pi} \int_{\rho_{lm}}^{\rho_c} \frac{dx}{\rho - x}. \tag{132}$$

The limiting process implied in Eq. (132) is completely analogous to that discussed in the ‘‘fundamental theorem of the calculus,’’ where the area under a curve, approximated by the sum of narrow rectangular strips, approaches the definite integral as the number of increments approaches infinity.

The lower limit of integration,  $\rho_{lm}$  will be chosen, in a way we describe shortly, to lie very nearly midway between  $x_{lm}$ , the last pole contained in the discrete sum, and  $x_{l,m+1}$ , the first pole included in the continuum approximation. The top endpoint of the integration of (132) is  $\rho_c = i/\sqrt{3}$ , as one can see from the sketch in Fig. 5(a).

In like manner, we find that the contribution from the right poles not included in (127) can be approximated by

$$\Delta\Pi_{rm} = \frac{e^{-i\pi/6}}{i\pi b^{1/3}} \sum_{n=m+1}^q \frac{K_n}{\rho - x_{rn}^{(0)}} \approx \frac{1}{i\pi} \int_{\rho_c}^{\rho_{rm}} \frac{dx}{\rho - x}. \tag{133}$$

Summing (132) and (133) to get the total continuum contribution from left and right poles we find

$$\Delta\Pi_m = \Delta\Pi_{lm} + \Delta\Pi_{rm} = \frac{1}{i\pi} \int_{\rho_{lm}}^{\rho_{rm}} \frac{dx}{\rho - x} = \frac{i}{\pi} \ln\left[\frac{\rho - \rho_{rm}}{\rho - \rho_{lm}}\right]. \tag{134}$$

As we shall discuss below, the contribution  $\Delta\Pi_c$  of the center poles is very small and can be neglected, so for  $\lambda \rightarrow 0$ , the  $m$ -pole approximation to the impedance (114) is

$$\Pi = \Pi_{lm} + \Pi_{rm} + \frac{i}{\pi} \ln\left[\frac{\rho - \rho_{rm}}{\rho - \rho_{lm}}\right], \tag{135}$$

with  $\Pi_{lm}$  and  $\Pi_{rm}$  given by (126) and (127).

Although the center contribution (134) was obtained for the special case of  $\lambda = 0$ , it is also an excellent approximation when  $\lambda \neq 0$ . Figure 5(c) shows the location of the poles  $x_n$  and the pole residue lines  $(\langle 1|n\rangle)^2$  for  $b = 10^5$  and  $\lambda = 0.122$ . It can be seen that for  $n > 5$  the pole residue lines

form a continuous straight line which can be approximated accurately by a line integral. We choose the values of  $\rho_{lm}$  and  $\rho_{rm}$  to ensure the validity of (111). Substituting (135) into (111) we find,

$$\rho_{rm} - \rho_{lm} = 2\Delta\rho_m = 2 - \sum_{n=1}^m [\langle 1|ln\rangle\{ln|1\rangle + \langle 1|rn\rangle\{rn|1\rangle}. \quad (136)$$

Here we made use of the identity

$$\int_{-\infty}^{\infty} d\rho \ln \left[ \frac{\rho - \rho_{rm}}{\rho - \rho_{lm}} \right] = -i\pi(\rho_{rm} - \rho_{lm}). \quad (137)$$

Since both  $\rho_{lm}$  and  $\rho_{rm}$  are in the upper half of the complex  $\rho$  plane, a convenient way to verify (137), is to continue the integral from  $\rho = +\infty$  along the real axis around an infinite semicircle in the upper half of the complex  $\rho$  plane to  $\rho = -\infty$  along the real  $\rho$  axis. The integral around the infinite semicircle is readily shown to contribute an additional amount  $i\pi(\rho_{lm} - \rho_{rm})$  to the result. We can collapse this closed contour, consisting of the integral along the real  $\rho$  axis with a return path on an infinite semicircle in the upper  $\rho$  plane, to an integral slightly outside the straight line cut from  $\rho_{lm}$  to  $\rho_{rm}$ . The integral about the cut is readily shown to yield  $2\pi i(\rho_{lm} - \rho_{rm})$ . Both integrals must give the same answer, since the integrand has no singularities between the two closed contours. Equating the two answers gives (137).

We choose the endpoint  $\rho_{lm}$  to lie as close as possible to the midpoint,  $(x_{lm} + x_{l,m+1})/2$ , of  $x_{lm}$ , the last discrete pole included in (115) and  $x_{l,m+1}$ , the first pole included in the continuum. Similarly, we choose the other endpoint  $\rho_{rm}$  to lie as close as possible to the midpoint  $(x_{rm} + x_{r,m+1})/2$ . The sum of the squared distances of  $\rho_{lm}$  and  $\rho_{rm}$  from the respective midpoints is minimized, subject to the constraint (136), when

$$\rho_{rm} + \rho_{lm} = 2\bar{\rho}_m = \frac{1}{2}(x_{lm} + x_{l,m+1} + x_{rm} + x_{r,m+1}). \quad (138)$$

Then the left and right ends of the cut in the complex  $\rho$  plane are

$$\rho_{lm} = \bar{\rho}_m - \Delta\rho_m \quad (139)$$

and

$$\rho_{rm} = \bar{\rho}_m + \Delta\rho_m. \quad (140)$$

For  $\lambda \rightarrow 0$  we can substitute (122) into (136) to find

$$\Delta\rho_m = 1 - \left( \frac{b_m}{b} \right)^{1/3}, \quad (141)$$

where the parameter  $b_m$  is

$$(b_m)^{1/3} = \frac{(3)^{1/2}}{2} \sum_{n=1}^m K_n. \quad (142)$$

Since we want the separation of the endpoints of the cut to be positive, (141) implies that  $b_m$  is the minimum value of  $b$

for which the  $m$ -pole approximation can be expected to work well. Substituting (118) into (138) we find for  $\lambda \rightarrow 0$ ,

$$\bar{\rho}_m = \frac{i}{4b^{1/3}}(-a'_m - a'_{m+1}). \quad (143)$$

We have assumed that the infinite number of center poles, located at the positions  $x_{cn}$  on the imaginary axis, make a negligible contribution to (114). To judge the size of their contribution we calculate for  $b = 1000$  the first few residues of the center poles:  $(c2|1)^2 = -9.1 \times 10^{-3}$ ,  $(c3|1)^2 = 3.7 \times 10^{-5}$ ,  $(c4|1)^2 = -3.6 \times 10^{-7}$ ,  $(c5|1)^2 = 5.5 \times 10^{-9}$ , etc. These numbers should be compared with the rigorous sum rule given by (111). Since the squared coefficients  $(cn|1)^2$  are very small and alternate in sign, we conclude that most of the contribution to (140) comes from the left and right poles. The values of  $(cn|1)^2$  are even smaller for much larger values of  $b$  in our experiments.

For future reference, the roots  $a'_n$ , the coefficients  $K_n$  and the minimum field inhomogeneities  $b_m$ , are listed in Table II.

When  $\lambda \neq 0$ , we find the poles  $x_{ln}$  and  $x_{rn}$  by converting (96) to a matrix equation with the aid of (104)

$$\sum_{k=1}^{\infty} (g|X|k)(k|n\rangle = (g|n\rangle x_n \quad (144)$$

with  $g = 1, 2, 3, \dots, \infty$ . It is not practical to solve the infinite-dimensional matrix equation (144), but since the matrix is nearly diagonal, it suffices to truncate (144) to include  $p$  left states  $|ln\rangle$  and  $p$  right states  $|rn\rangle$  with  $n = 1, 2, 3, \dots, p$ . For use with the  $m$ -pole approximation discussed above, we assume that  $m \ll p \ll q$ . In practice,  $m = 4$  and  $p = 10$  are large enough to give results practically indistinguishable from those obtained with much larger values of  $m$  and  $p$ . With contemporary mathematics packages and computers, one can readily solve the complex eigenvalue equation

$$\sum_{k=1}^p (lg|X|lk)(lk|ln\rangle = (lg|ln\rangle x_{ln}, \quad (145)$$

where  $g \leq p$ . The matrix is

$$(lg|X|lk) = (lg|X^{(0)}|lk) + \lambda(lg|X^{(1)}|lk). \quad (146)$$

From (95) we see that

$$(lg|X^{(0)}|lk) = \delta_{gk} x_{lg}^{(0)}, \quad (147)$$

and from (94) we see that

$$\begin{aligned} (lg|X^{(1)}|lk) &= \int_{-1}^1 d\xi \phi_{lg}(\xi) [F(\xi) - 1] \phi_{lk}(\xi) \\ &+ \int_{-1}^1 d\xi' \int_{-1}^1 d\xi \phi_{lg}(\xi') T(\xi' - \xi) \phi_{lk}(\xi). \end{aligned} \quad (148)$$

Analogous expressions to (145)–(147) hold with  $l \rightarrow r$ , that is for the right poles and right eigenfunctions.

When evaluating the matrix elements (148) by numerical integration, it is important to account for the logarithmic singularity of  $T$ ,

$$T(\xi) \rightarrow \frac{1}{\pi\beta} \left\{ \ln \left( \frac{8\beta}{|\xi|} \right) - 2 \right\}, \quad \text{as } |\xi| \rightarrow 0. \quad (149)$$

$F(\xi)$  is defined by (64) as an integral of  $T$ , so there is a related logarithmic singularity of  $F'(\xi)$ , at  $\xi = \pm 1$ . The singularities of  $T$  and  $F$  can be recognized in Fig. 2.

The  $m$  most slowly damping eigenvalues  $x_{ln}$  obtained by the numerical solution of (145) are used as poles in (115). To find the factors  $\langle 1|ln\rangle\{ln|1\rangle$  needed for (115) and (136), we can use eigenvectors  $(lg|ln\rangle)$  to write

$$\langle 1|ln\rangle = \{ln|1\rangle = \sum_{k=1}^p \langle 1|lk\rangle(lk|ln\rangle), \quad (150)$$

with  $\langle 1|lk\rangle = (lk|1\rangle$  given very nearly by (122). An equation analogous to (149) for  $\langle 1|ln\rangle$  holds for  $\langle 1|rn\rangle$ . To get  $\rho_{rm}$  and  $\rho_{lm}$  for the evaluation of (135) we use (136), (138), (139), and (140).

The results of our calculations of  $\Pi(\rho)$  for  $b = 10^5$  and  $\lambda = 0.122$  are shown in Figs. 4(b) and 4(c). We diagonalize a  $10 \times 10$  matrix and use the first 4 discrete poles. The effect of self-interactions makes the impedance asymmetric, always enhancing the peak near  $\rho = 1$ . This allows masing for larger field gradients if the Larmor frequency of the spins is less than the coil resonance frequency. The impedance is not significantly affected by self-interaction effects away from  $\rho = \pm 1$ .

For practical estimates of the largest magnetic field gradient for which masing can occur, it is sufficient to study the contribution to the impedance of the rightmost pole, which dominates the impedance peak near  $\rho = 1$ . The maximum value of the real part of the impedance is nearly given by

$$\text{Max}[\text{Re } \Pi] \approx \frac{\text{Re}\{1|rn\rangle^2}{\pi \text{Im } x_{r1}}. \quad (151)$$

Figure 6 shows the dependence of the maximum real value of  $\Pi$  on  $\lambda$  and  $b$ . We note that in the absence of spin self-interaction ( $\lambda = 0$ )  $\text{Max}[\text{Re } \Pi] = 1.57$  independent of  $b$  as long as  $b \gg 1$ . Thus, the effect of spin self-interaction is to enhance the negative resistance of the spins by 2 orders of magnitude over the range of  $\lambda$  studied. Our approximation becomes more difficult to implement for larger values of  $\lambda$  because we need to diagonalize larger matrices. For  $\lambda > 0.2$  we need a  $20 \times 20$  matrix to obtain results accurate to 10%. In addition, the basis eigenfunctions given by Eq. (119) become large and highly oscillatory, making the calculation of the integrals in Eq. (148) numerically difficult.

In our analysis of (21), we have assumed a negative nuclear moment  $\mu_K < 0$ , as is the case for both  $^3\text{He}$  and  $^{129}\text{Xe}$ . In the case of positive nuclear moments like the proton,  $\mu_K > 0$ . The minor changes needed to account for a positive  $\mu_K$  can be deduced from inspection of (21). The gyromagnetic ratio (3) is negative, the mean Larmor frequency  $\bar{\omega}_L$  is negative, the positive resonance frequency  $\omega -$  of order  $\omega \approx -\bar{\omega}_L -$  causes a large enhancement of  $\tilde{M}_-$  rather than  $\tilde{M}_+$ . Equation (47) becomes

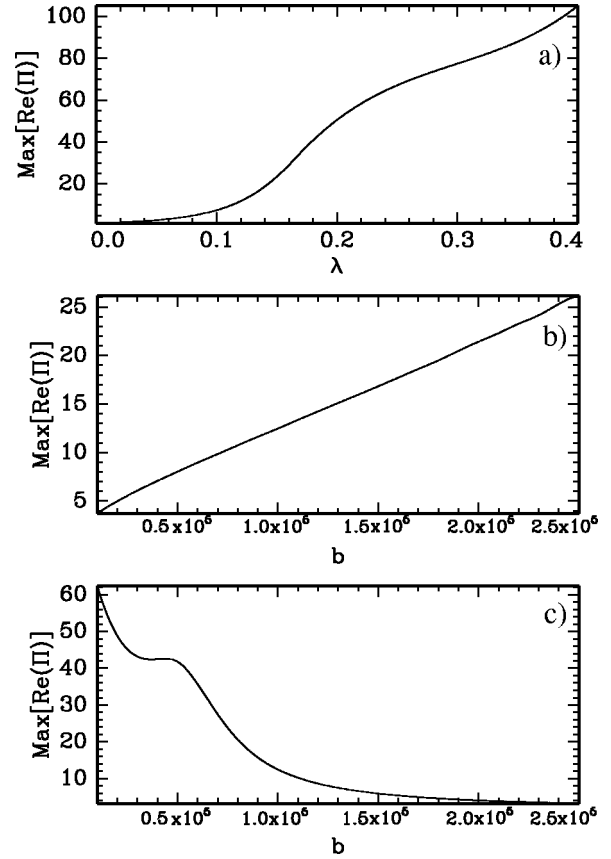


FIG. 6. Dependence of  $(\text{Re}\Pi)_m$  on  $\lambda$  and  $b$ . Plot (a) shows the dependence on  $\lambda$  for a fixed  $b = 10^5$ . Plot (b) shows the dependence on  $b$  for a fixed  $\lambda = 0.122$ . Plot (c) shows the dependence on  $b$  for a fixed  $^3\text{He}$  polarization and density. In this case  $\lambda \propto b^{-1}$ . We set  $\lambda = 0.122$  at  $b = 10^5$ .

$$\tilde{M}_- = \frac{-i\omega_q P \Omega \tilde{H}_{C-}}{2gl^2 a^2} \mu. \quad (152)$$

$\mu$  continues to satisfy (65), so  $\mu$  and  $\Pi$  are given by the same expressions as for  $\mu_K < 0$ , but the impedance is

$$Z_M = \frac{\omega W P}{b} \Pi. \quad (153)$$

Thus for positive nuclear moments, negative polarization  $P$  is needed to make the real part of the impedance negative and lead to masing. This follows since for  $\mu_K > 0$ , the emission of Larmor-frequency photons causes the spin polarization to increase.

### III. EXPERIMENTS

#### A. Apparatus

Experiments were performed with a laser-polarized sample of  $^3\text{He}$ . The apparatus is sketched in Fig. 7. We fabricated a special cell, consisting of two chambers, the pumping cell and the maser cell. The maser cell, a right circular cylinder, had an inner diameter (ID)  $2a = 9$  mm, and an inside length  $2l = 6.8$  cm. The ends of the cylinder were made as flat and as parallel to each other as possible. A thin connection tube, which had a 2.5 mm ID at the entrance

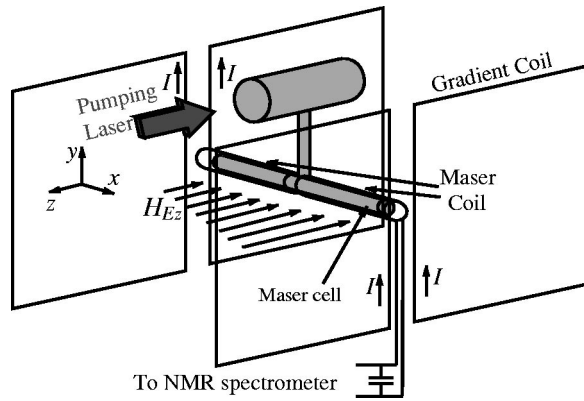


FIG. 7. Experimental apparatus for studies of the Larmor-frequency maser. A uniform magnetic field in the maser cell was created by a set of Helmholtz coils, which are not shown. A magnetic field gradient was produced by four square loops with current directions indicated on the figure. The magnetic field gradient is greatly exaggerated. A two-section solenoid, the maser coil, surrounded the maser cell and could be connected in series with a capacitor to form an  $LC$  circuit with a resonant frequency of 80.1 kHz. The voltage across the capacitor was monitored with an NMR spectrometer to determine the onset of masing.

to the maser cell, joined the maser cell to the pumping cell. The cell was filled with 9.6 atm. of  $^3\text{He}$  and 50 Torr of  $\text{N}_2$ , measured at room temperature. It also contained a few mg of Rb metal to provide Rb vapor for spin-exchange optical pumping. The diffusion time for  $^3\text{He}$  between the pumping cell and the maser cell was approximately 1 h. The spin relaxation time of  $^3\text{He}$  was about 20 h. The pumping cell was placed in an oven where it was heated by flowing hot air to 185 °C. A 100-W fiber-optic-coupled laser array was used for optical pumping. The optical pumping time constant was about 4 h. When the pumping cell was hot, more gas was pushed into the maser cell, which was at a temperature of 50 °C. Based on the ratio of the volumes and temperatures we calculated that the operating density of the gas in the maser cell was 1.37 times larger than the density when the pumping and maser cells had the same temperature. This calculation was verified by observing the decreasing NMR signal as the pumping cell was cooled down. The  $^3\text{He}$  diffusion constant in the maser cell was [13]  $D=0.181\text{ cm}^2/\text{s}$ .

The maser cell was wrapped with a maser coil, consisting of two identical solenoidal sections connected in series and separated by 0.8 cm at the center of the cell to provide room for the connecting tube. Each solenoidal section had 168 turns of wire. The turns had a mean diameter of 1.7 cm, and they were uniformly spaced along a 5.2 cm length. The total inductance  $L$  of the solenoid was 276  $\mu\text{H}$ . For observation of masing oscillations the solenoid was connected to a capacitor  $C$ . The measured resonance frequency was  $f_0 = \omega_0/(2\pi) = 80.1\text{ kHz}$  and the quality factor was  $Q=26$ .

A set of Helmholtz coils created a uniform magnetic field that was set at values ranging from 18 to 34 G for measurements of the inhomogeneity thresholds for masing as a function of the Larmor frequency. The applied field gradient was produced by four current loops, carrying the same current  $I$  and arranged as sketched in Fig. 7. The gradient  $\partial H_z/\partial x$  produced by the coils is shown on Fig. 8. It varied by less than 7% within  $\pm 2\text{ cm}$  from the center of the coil, but in-

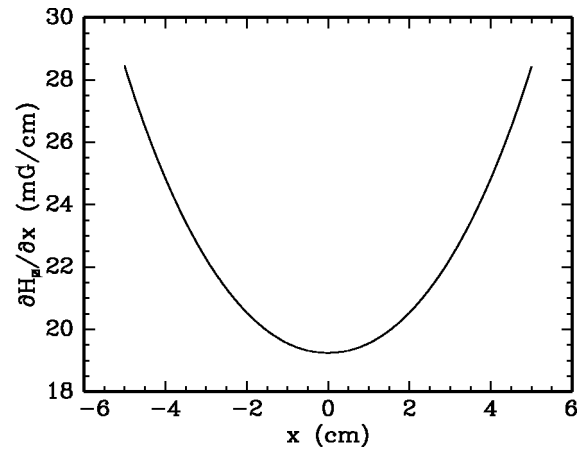


FIG. 8. Magnetic-field gradient produced by the gradient coil with a typical current equal to 2 A.

creased by 25% at a distance of 3.4 cm from the center. The value of the inhomogeneity parameter  $b$  was calculated using Eq. (43). As shown in Fig. 3, for large values of  $b$  masing occurs in a thin transverse slice with a width of approximately 3 mm. The position of the masing slice at masing threshold depends on the mean Larmor frequency and on the resonance frequency of the maser coil. When the mean Larmor frequency was changed, the gradient coil was translated along the  $x$  axis so its center was within 2 cm of the location of the masing slice. We verified that the masing threshold was not sensitive to translations of the gradient coil when its center was close to the masing slice. The ambient gradients were on the order of 0.3 mG/cm.

Saam [18] showed that the diamagnetism of the glass walls of the cell can distort the edge enhancement. Within the glass, the magnetization is  $M_{gz} = \chi_g \bar{H}_{Ez}$  where the magnetic susceptibility of glass is  $-\chi_g \approx 10^{-6}$ . The gradient due to the magnetization of the glass reaches a maximum of 0.6 mG/cm near the walls of the cell, which is much less than typical applied gradients of 20 mG/cm, or the gradients due to the magnetization of the  $^3\text{He}$  nuclei.

Data were acquired as follows. After 10 h of optical pumping the  $^3\text{He}$  polarization reached an equilibrium value of about 40%. A large magnetic field gradient of 40 mG/cm was applied with the gradient coils. The maser solenoid was connected to the capacitor and the voltage across the solenoid was monitored using a nuclear magnetic resonance (NMR) spectrometer. The gradient was gradually reduced until the masing oscillations could be observed. The critical gradient corresponding to the onset of masing was recorded and the frequency  $\omega$  of the oscillations was measured using a frequency counter. Then the gradient was increased to stop the masing, the uniform magnetic field was changed to a new value, resulting in a new mean Larmor frequency  $\bar{\omega}_L$  and the process was repeated. The maser frequency  $\omega$  was always close to the mean Larmor frequency  $\bar{\omega}_L$ . In this way we mapped out the inhomogeneity threshold for the onset of masing as a function of the maser frequency  $\omega$  for a constant resonance frequency  $\omega_0$  of the coil and a constant  $^3\text{He}$  polarization. Care was taken to keep the amplitude of the masing signal small, to prevent significant losses of  $^3\text{He}$  polarization. Periodic measurements of  $^3\text{He}$  polarization confirmed that it was constant to within 3%.

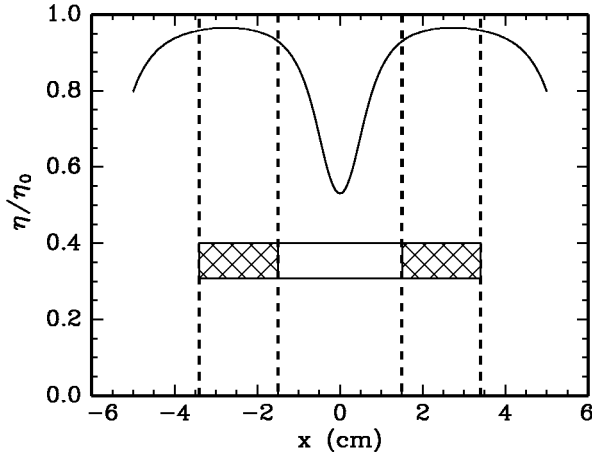


FIG. 9. Ratio  $\eta(x)/\eta_0$  of the axial magnetic field per unit current produced by the maser coil to the field per unit current, produced by an ideal solenoid. The outline of the maser cell is also shown. The volume  $\Omega_m$  is hatched.

The measurements of the  $^3\text{He}$  polarization were done using a low frequency pulsed NMR spectrometer with a high-impedance pre-amplifier. For this measurement the resonating capacitor was disconnected from the maser coil and the current source was removed from the gradient coil. The polarization of  $^3\text{He}$  was determined from the initial amplitude of the free-induction-decay (FID) signal following an excitation pulse to the solenoid. In the limit of small tipping angle, one can show that the initial peak amplitude  $V_F$  of the FID voltage  $V_M$  of (74), in cgs units of statvolts, is given by

$$V_F = \lim_{t \rightarrow 0} \max V_M(t) = \frac{G \omega \tau_p I_p \gamma \mu_K [\text{He}] P}{2} \int_{\Omega} \eta^2 d^3 \mathbf{r}, \quad (154)$$

where  $G$  is a dimensionless instrumental gain,  $I_p$  is the peak amplitude of a rectangular pulse of alternating current, of duration  $\tau_p$  which flows through the maser coil just before  $t=0$ , and is used to provide the initial transverse magnetization  $M_x$  of (74). The field per unit current  $\eta = \eta(\mathbf{r})$  is a function of position in the cell and can be defined by

$$\eta(\mathbf{r}) = \frac{\partial H_x}{\partial I}. \quad (155)$$

For an ideal, infinite solenoid  $\eta = \eta_0$  is independent of position, as discussed in connection with Eq. (38) Direct measurements of  $V_F$ ,  $G$ ,  $I_p$ , and  $\tau_p$  allowed us to determine the factor

$$S = [\text{He}] P \int_{\Omega} \eta^2 d^3 \mathbf{r} \quad (156)$$

of Eq. (154) with an accuracy of 3%. The variation of

$$\eta(x) = \frac{1}{\pi a^2} \int dy dz \eta(\mathbf{r}) \quad (157)$$

along the axis of the cell can be calculated from the known geometry of the solenoid and is shown in Fig. 9. For the inhomogeneous-broadening regime, masing occurs for spins in a thin slice, transverse to the cell axis. For most of our

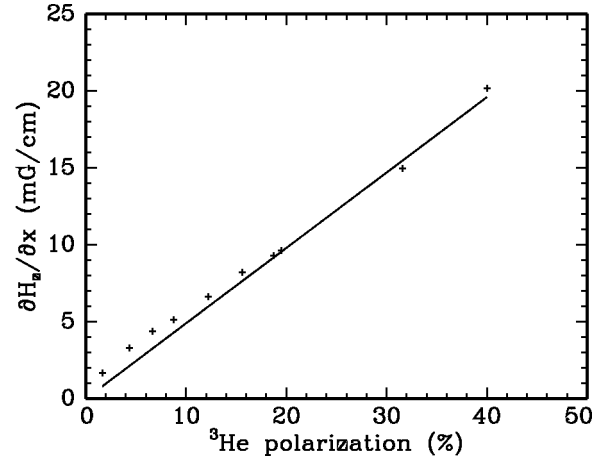


FIG. 10. Dependence of the masing threshold on the polarization of  $^3\text{He}$  for masing frequency equal to the coil resonance frequency. The solid line is given by Eq. (73) without any free parameters.

data this slice is close to one of the two flat end walls of the maser cell. Therefore, it is apparent from Fig. 9 that the value of  $\eta$  which is relevant for the maser threshold is larger than the average value over the whole cell. Near the ends of the cell  $\eta$  is fairly constant, it varies by less than 8% between  $x=1.5$  and  $x=3.4$ . We account for the non-uniformity of  $\eta$  by replacing  $\eta_0$  in the theoretical model by

$$\eta_m = \left( \frac{1}{\Omega_m} \int_{\Omega_m} \eta^2 d^3 \mathbf{r} \right)^{1/2}. \quad (158)$$

Here  $\Omega_m$  is the volume where the maser slice is located for most conditions, between  $x = -3.4$  cm and  $x = -1.5$  cm or between  $x = 1.5$  cm and  $x = 3.4$  cm.

The value of the maser inductance  $W$  is determined from the NMR signal  $S$  using Eq. (44)

$$W = \frac{\hbar K \pi \gamma^2 l^2 S}{4D} C_\eta, \quad (159)$$

where the coil correction factor  $C_\eta$

$$C_\eta = \frac{\Omega}{\Omega_m} \frac{\int_{\Omega_m} \eta^2 d^3 \mathbf{r}}{\int_{\Omega} \eta^2 d^3 \mathbf{r}} = 1.19 \quad (160)$$

is calculated numerically. The self-interaction parameter  $\lambda$  is determined from Eqs. (68), (156), and (158).

To independently check our results, we also measured the Rb Larmor-frequency shift [14] due to spin exchange with  $^3\text{He}$  in the pumping cell. The shift is proportional to the polarization and density of  $^3\text{He}$ . This measurement indicated that the polarization of  $^3\text{He}$  in the pumping cell was higher by a factor of 1.07 than in the maser cell, which is consistent with polarization loss during diffusion from the pumping cell to the maser cell.

## B. Results

Our experimental results for the threshold of the maser oscillations are shown in Figs. 10 and 11. In Fig. 10 we show

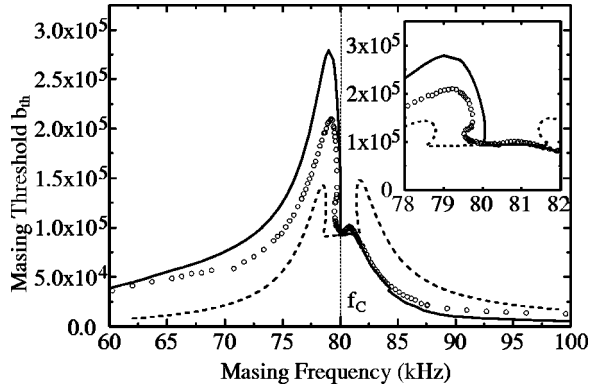


FIG. 11. Comparison of the masing threshold data (circles) with theoretical calculations for  $\lambda=0.122$  (solid line) and  $\lambda=0$  (dotted line). There are no free parameters. The inset shows the resonance region in more detail.

the dependence of the maser threshold gradient on the value of the  $^3\text{He}$  polarization. For this set of data the maser frequency  $\omega$  was set close to the coil resonance frequency  $2\pi f_0$ . As discussed in relation to Eq. (73), this case is particularly easy to analyze. The threshold value of the magnetic field gradient, given by Eq. (73), is proportional to the  $^3\text{He}$  polarization  $P$  and is independent of the diffusion constant  $D$ . Note that these properties are qualitatively different from the properties of a motionally-narrowed maser, for which the threshold gradient is proportional to  $P^{1/2}$  and inversely proportional to  $D$ . We expect that Eq. (73), derived in the absence of spin-interactions, should remain quite accurate even if they are taken into account. As can be seen from Figs. 4(a), and 4(b), the value of  $\Pi$  is unaffected by the addition of spin self-interactions near  $\rho=0$ . Indeed, we find that our data are in excellent agreement with the threshold gradient given by Eq. (73), which is shown in Fig. 10 by the solid line.

More complicated behavior of the spin maser is shown in Figure 11. Here we map out the frequency dependence of the maser threshold for a constant value of the  $^3\text{He}$  polarization. On the horizontal axis we plot the masing frequency  $\omega$ , measured directly with a frequency counter, and on the vertical axis the threshold value of the inhomogeneity parameter  $b_{th}$  which corresponds to the onset of the masing. Note that  $b \gg 1$  for all our data. The  $^3\text{He}$  polarization was equal to 35% for this set of data. Small variations of the polarization, on the order of 3%, were corrected for by assuming that  $b_{th} \propto P$ , which follows from Eq. (39) if the dependence of  $\Pi$  on  $b$  is relatively weak. For most data shown in Fig. 11 the magnetic field gradient was reduced until maser oscillations could be observed. Reducing the gradient even further resulted in exponentially growing masing. This behavior is to be expected, since for smaller magnetic field gradient the spins have a longer dephasing time, and thus have a greater chance to contribute coherently to the build-up of maser oscillations. However for a narrow range of frequencies shown in the inset of Fig. 11, this behavior was reversed. The maser oscillations could be started by increasing the magnetic field gradient past a certain threshold. This counter-intuitive behavior is due to the complex behavior of  $\Pi(\rho)$  near  $\rho = \pm 1$ . The area enclosed by the experimental data and the

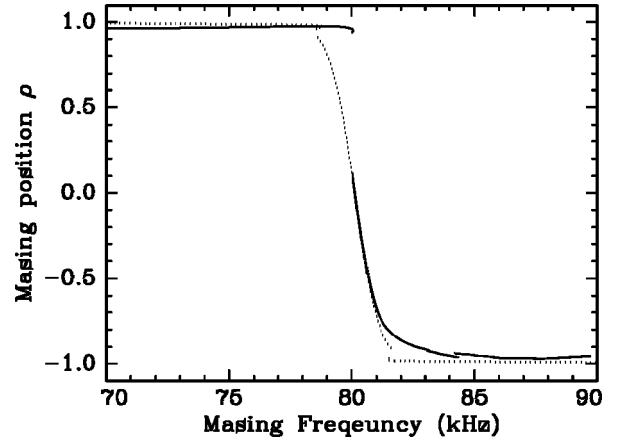


FIG. 12. Calculated relative position of the maser mode  $\rho$  vs maser frequency for  $\lambda=0.122$  (solid line) and  $\lambda=0$  (dotted line).

bottom axis,  $b=0$ , corresponds to the unstable condition where masing will occur. Masing cannot occur for any other region of the  $b-f$  plane.

Two theoretical curves are also shown in Fig. 11, with and without the effect of the self-interactions. The threshold gradient and the frequency of the masing oscillations are determined from the equation

$$Z_C(\omega) + Z_M(\omega, b, \bar{\omega}_L) = 0. \quad (161)$$

To solve Eq. (161) we first calculate  $\Pi(\rho)$  for a given  $b$  using the formalism in Sec. II C. We diagonalize a  $10 \times 10$  matrix  $(lg|X|lk)$  given by (145) and constructed according to (146) with the ten most slowly damping, unperturbed left eigenfunctions (119) to find the perturbed pole locations  $x_{lm}$  and residue amplitudes  $\langle 1|In \rangle$ , given by (150). We make a similar calculation using the ten most slowly damping, unperturbed right eigenfunctions. We use (136) and (138) to calculate  $\rho_{lm}$  and  $\rho_{rm}$ .  $\Pi(\rho)$  is then evaluated with (114)–(116) and (134), with  $m=4$ . Then we find real values of  $\omega$  and  $\rho$  for which both real and imaginary parts of Eq. (161) are satisfied. The calculation is repeated for many values of  $b$ , giving a curve in the  $b-f$  space, which can be directly compared with data shown in Figure 11. In addition, we obtain the value of  $\rho$ , which relates the masing frequency  $\omega$  to the average Larmor frequency  $\bar{\omega}_L$  set by the magnetic field,  $\omega = \bar{\omega}_L + \rho gl$ .  $\rho$  also gives the location of the masing slice where the transverse magnetization is peaked,  $x \approx \rho l$ . The theoretical dependence of  $\rho$  on the masing frequency is shown in Fig. 12. The discontinuities in the  $\rho$  vs.  $f$  curve correspond to the discontinuities in the slope of  $b_{th}$  vs.  $f$  curve. At these points the preferred configuration of the precessing magnetization which has the largest gain for masing changes discontinuously.

All of the general features of the data are very well reproduced by our model. In particular, the model and the data show a large increase of the threshold gradient for slight detuning of the masing frequency away from the coil resonance frequency. This increase can be attributed to the edge-enhancement effects, which are also seen in the spin impedance shown in Fig. 4. The effect of self-interactions is to greatly increase the peak for masing frequency below the coil resonance frequency and reduce or eliminate the peak

for masing frequency above the resonance frequency. Both the model and the data have a region where maser oscillations can be started by increasing the magnetic field gradient. Thus, our theory of inhomogeneously broadened spin maser correctly explains all of its unusual properties.

The quantitative agreement between our data and the theory, which does not have any free parameters, is also reasonably good. The only disagreement is in the height of the peak on the low side of the coil resonance frequency. We believe that the largest limitation of our theory is due to its 1-dimensional nature. We neglect the variation of the magnetization in the plane perpendicular to axis of the cylinder. Even for perfect experimental conditions, some transverse variation of  $\mathbf{M}$  can be expected due to the self-interaction field near the ends of the cell. In addition, if the end surfaces of the cell are not perfectly flat or not perpendicular to the direction of the magnetic field gradient, the accuracy of the one-dimensional approximation is further reduced. Because masing occurs in a very thin slice with a thickness of only 3 mm, small imperfections of the end walls of the cell can affect the boundary condition.

#### IV. CONCLUSIONS

In this paper we have presented the first theoretical and experimental treatment of a spin maser in the regime of inhomogeneous broadening. We have considered in detail the threshold behavior of the maser and we have determined the region in the parameter space where masing oscillations can occur. The behavior of the threshold value of the magnetic field gradient is counterintuitive. It reaches its maximum value when the mean Larmor frequency is detuned away from the resonance frequency of the maser coil. If a magnetic field gradient is such that masing cannot occur, sufficiently decreasing the gradient will lead to masing. However, in certain ranges of maser frequencies, non-masing field gradients exist which lead to masing if they are decreased or *increased* sufficiently. We also present the first detailed ac-

count of the effect of magnetic self-interactions on the spin maser. Self interactions significantly enhance the range of parameters where masing oscillations can occur.

We use a theoretical approach based on the eigenfunctions and eigenvalues of the non-Hermitian spin evolution operator. The impedance is proportional to a sum on poles, located at the complex eigenvalues of the the evolution operator. Only the first few of the infinite number of poles in the sum need to be explicitly included. The contribution of the remaining poles can be accounted for with great precision by replacing the sum with an integral over a continuous line of poles. In spite of the unusual properties of the eigenfunctions, for example, peak amplitudes that are many orders-of-magnitude smaller for eigenfunctions localized near the cell edges than for interior eigenfunctions, which have eigenvalues close to the three-fold vertex of the eigenvalue spectrum, no serious difficulties were encountered in numerical computations.

In addition to its intrinsic interest, our work allows one to estimate the masing threshold in applications of dense hyperpolarized gases and liquids. In most cases masing is an undesirable effect which reduces nuclear polarization. For example, there is strong evidence that masing was limiting the  $^3\text{He}$  polarization during a recent measurement of the neutron spin structure function at SLAC [14,23]. Masing can be entirely avoided by polarizing the spins in the low energy state. Otherwise, it can be suppressed by increasing magnetic field gradient, setting the spin Larmor frequency above the coil resonance frequency and reducing the coupling of the spins to the coil.

#### ACKNOWLEDGMENTS

We would like to thank Ioannis Kominis for assistance with the experiment. This work was supported by the U.S. Air Force Office of Scientific Research and the National Science Foundation.

- 
- [1] T.G. Walker and W. Happer, *Rev. Mod. Phys.* **69**, 629 (1997).
  - [2] J. Becker *et al.*, *Nucl. Instrum. Methods Phys. Res. A* **346**, 45 (1994).
  - [3] H.G. Robinson and T. Myint, *Appl. Phys. Lett.* **5**, 116 (1964).
  - [4] M.G. Richards, B.P. Cowan, M.F. Secca, and K. Machin, *J. Phys. B* **21**, 665 (1988).
  - [5] T.E. Chupp, R.J. Hoare, R.L. Walsworth, and B. Wu, *Phys. Rev. Lett.* **72**, 2363 (1994).
  - [6] G.D. Cates, S.R. Schaefer, and W. Happer, *Phys. Rev. A* **37**, 2877 (1988).
  - [7] D.D. McGregor, *Phys. Rev. A* **41**, 2631 (1990).
  - [8] K. Abe *et al.* (E-154 Collaboration), *Phys. Rev. Lett.* **79**, 26 (1997).
  - [9] M.S. Albert *et al.*, *Nature (London)* **370**, 199 (1994).
  - [10] J.R. MacFall *et al.*, *Radiology* **200**, 553 (1996).
  - [11] J.P. Mugler *et al.*, *Magn. Reson. Med.* **37**, 809 (1997).
  - [12] K.L. Sauer, R.J. Fitzgerald, and W. Happer, *Chem. Phys. Lett.* **277**, 153 (1997).
  - [13] J. Kestin, K. Knierim, E.A. Mason, B. Najafi, S.T. Ro, and M. Waldman, *J. Phys. Chem. Ref. Data* **13**, 229 (1984).
  - [14] M.V. Romalis and G.D. Cates, *Phys. Rev. A* **58**, 3004 (1998).
  - [15] E. Purcell, *Electricity and Magnetism; Berkeley Physics Course — Volume 2* (McGraw-Hill, New York, 1963).
  - [16] A. Apelblat, *Table of Definite and Infinite Integrals* (Elsevier, Amsterdam, 1983), p. 225.
  - [17] J. D. Gaskill, *Linear Systems, Fourier Transforms and Optics* (Wiley, New York, 1978).
  - [18] B. Saam, N. Drukker, and W. Happer, *Chem. Phys. Lett.* **263**, 481 (1996).
  - [19] P.T. Callaghan, A. Coy, L. Forde, and C. Rofe, *J. Magn. Reson., Ser. A* **101**, 347 (1993).
  - [20] T.M. deSwiet and P.N. Sen, *J. Chem. Phys.* **100**, 5597 (1994).
  - [21] S.D. Stoller, W. Happer, and F.J. Dyson, *Phys. Rev. A* **44**, 7459 (1991).
  - [22] L. D. Landau and E. M. Lifshitz, *Electrodynamics of Continuous Media* (Pergamon Press, Oxford, 1984), 2nd ed.
  - [23] M. V. Romalis, Ph.D. thesis, Princeton University, 1997 (unpublished).